Letter of Intent for ATLAS FP: A project to install forward proton detectors at 220 m and 420 m upstream and downstream of the ATLAS detector

Abstract

We present a proposal to build and install forward proton detectors at 220 m and 420 m from the interaction point on both sides of the ATLAS experiment. The detectors would be designed to operate at instantaneous luminosities of up to 10^{34} cm^{-2}s^{-1}. The primary goal is to enhance the ATLAS baseline physics program, particularly the search for, identify, and measure the properties of new particles such as Higgs bosons and supersymmetric particles. We aim to install the detectors during the winter 2010 shutdown. Total cost for the project is estimated to be 5M CHF, of which 1.5M CHF will be a cryogenic bypass at 420 m.

Contents

Executive Summary

This letter of intent outlines a proposal to upgrade the forward region at ATLAS by installing silicon and fast timing detectors 220 m and 420 m from the interaction point to detect intact final state protons scattered at small angles and with small momentum loss. The capability to detect *both* outgoing protons in diffractive and photoproduction processes allows for a rich QCD, electroweak, Higgs and beyond the Standard Model experimental program that has the potential to make unique measurements at the LHC. The installation of forward proton detectors at 420 m around both ATLAS and CMS was investigated in detail by the FP420 R&D Collaboration in Ref. [1]. In this document we summarize the results of the FP420 program adding ATLAS specific details where appropriate, and also summarize the plans to add a similar system at 220 m. Unlike the 420 m region, the 220 m region does not require a cryogenic bypass, as this region already has an exposed warm beam pipe.

At both the 420 m and 220 m locations, we propose to install movable beam pipes which will host silicon tracking and fast timing detectors (i.e. four independent detector stations). The system functions as a spectrometer, using the LHC dipole and quadrupole magnets to bend the scattered protons out of the beam envelope. It is necessary to measure both the distance from the beam and the angle of the proton tracks relative to the beam with high precision in order to reconstruct the mass of the central system produced in ATLAS. The 420 m stations can detect protons with fractional momentum losses in the range $0.002 < \xi < 0.02$. 220 m stations provide complementary coverage in the range $0.02 < \xi < 0.2$. For events in which both protons are tagged, this corresponds to a range of central masses from ~ 80 GeV to beyond 1 TeV. At luminosities in excess of 2×10^{33} cm^{-2}s^{-1} it is necessary to measure the time of arrival of the protons with an accuracy of 20 ps to suppress experimental backgrounds. As the luminosity approaches 10^{34} cm^{-2}s^{-1}, resolutions of 10 ps or better become necessary.

A prime process of interest is Central Exclusive Production (CEP), $pp \to p + \phi + p$, in which the central system ϕ may be a single particle such as a Higgs boson. Observation of a new particle in the CEP channel allows for a direct determination of its quantum numbers, since to a good approximation only 0^{++} central systems can be produced in this way. Furthermore, tagging both protons allows the mass of the centrally produced system ϕ to be reconstructed with a resolution (σ) between 2 GeV and 3 GeV *per event* if both protons are tagged at 420 m, irrespective of the decay products of the central system. For $m_\phi > 160$ GeV, it becomes necessary to tag one proton at 420 m and one at 220 m. The mass resolution for these 'asymmetric' events $\sigma \sim 5$ GeV. The cross section for the CEP of a Standard Model Higgs boson is predicted to be in the few femtobarn range, rising to 10s of femtobarns in certain areas of MSSM parameter space. The proposed upgrades must therefore be designed to operate at the highest LHC instantaneous luminosities of 10^{34}cm^{-2}s^{-1}. As well as CEP, the photoproduction process $\gamma\gamma \to \phi$ is also a promising discovery channel; 420 m and 220 m proton tagging will allow for precision measurements of photon-photon interactions well beyond the electroweak scale for the first time. In certain areas of mSUGRA / CMSSM parameter space (for example the LM1 point), the pair production of supersymmetric particles may allow for high precision measurements of the sparticle masses. Single diffractive and γp processes are also of immense interest in this energy range, requiring only one proton tag per event.

The outline of this document is as follows. We summarize the physics motivation for the proposed upgrade in Chapter 1. In Chapter 2 we describe the acceptance and mass resolution of the proposed 220 m + 420 m system at ATLAS, and consider alignment strategies for the detectors, which have a direct impact on the mass resolutions achievable with the system. In Chapter 3 we briefly review the solutions developed by FP420 for the installation of proton detectors at 420 m in the cold region of the LHC, and the installation of similar detectors at 220 m. In Chapter 4 we describe the Hamburg moving beam pipe solution for housing both silicon tracking and fast timing detectors at both 220 m and 420 m, and the backgrounds that will ultimately determine the closest distance of approach to the LHC beams. Chapter 5 describes the silicon detector technology chosen for both 220 m and 420 m. In Chapter 6 we describe the fast timing detectors necessary for operation at higher luminosities. Chapter 7 describes a proposed L1 trigger system for the 220 m detectors. We present a preliminary cost estimate and conclusions in Chapter 8.

Chapter 1

Physics Case for Forward Proton Detectors at ATLAS

1.1 Central exclusive production

The central exclusive production (CEP) of new particles has received a great deal of attention in recent years [2–17]. By central exclusive production, we refer to the process $pp \rightarrow p + \phi + p$ where the final state consists only of the central system ϕ and the outgoing intact protons,. This is shown schematically for Higgs boson production in Fig. 1.1. The '+' sign denotes the regions devoid of activity, often called rapidity gaps.

There are three important reasons why CEP is especially attractive for studies of new particles. Firstly, if the outgoing protons remain intact and scatter through small angles then, to a very good approximation, the primary active di-gluon system obeys a $J_z = 0$, C-even, P-even, selection rule [18]. Here J_z is the projection of the total angular momentum along the proton beam axis. This selection rule readily permits a clean determination of the quantum numbers of any new resonance. Secondly, because the process is exclusive, the energy loss of the outgoing protons is directly related to the invariant mass of the central system, allowing an excellent mass measurement irrespective of the decay mode of the central system [19]. Even final states containing jets and/or one or more neutrinos are measured with $\sigma_M \sim 2$ GeV/c^2. Thirdly, in many topical cases and in particular for Higgs boson production, a signal-to-background ratio of order 1 or better is achievable [6, 7, 14, 20, 21]. This ratio becomes significantly larger for Higgs bosons in certain regions of MSSM parameter space [7, 15, 16].
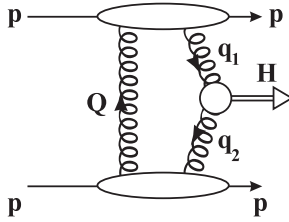
Figure 1.1: Central Exclusive Production (CEP) of a Higgs boson: $pp \rightarrow p + H + p$.

The CEP cross sections in the following discussion are calculated using the KMR model [4, 9]. The CDF collaboration has searched for evidence of the CEP process and observed a 6σ excess of events in the exclusive di-jet sample, $p\bar{p} \rightarrow p + jj + \bar{p}$ [22], at a rate consistent with the theoretical predictions. CDF has also observed several candidates for central exclusive di-photon production, $p\bar{p} \rightarrow p + \gamma\gamma + \bar{p}$, consistent with the predicted rates [23].

1.1.1 $h \rightarrow b\bar{b}$

As an example of what may be possible with ATLAS FP, we briefly review a detailed analysis carried out in Ref. [16], and extended Ref. [1], of the $h \rightarrow b\bar{b}$ channel in a specific MSSM scenario. The MSSM point chosen for this analysis is $m_A = 120$ GeV and tanβ=40. The lightest Higgs boson, h, has a mass of 119.5 GeV and the cross section×branching ratio is approximately 20 fb. ATLAS FP is particularly well suited to observing the Higgs sector in certain regions of MSSM parameter space; at high tanβ the CEP cross sections are in general enhanced with respect to the Standard Model and the branching ratio to $b\bar{b}$ can be as high as 90% if the light SUSY decay channels are not allowed. Furthermore, the $J_z = 0$ selection rule suppresses the irreducible $b\bar{b}$ continuum background significantly, thus enhancing the signal to background ratio [21] with respect to standard search channels. Finally, because the pseudo-scalar A cannot be produced in CEP, ATLAS FP will provide a clean measurement of the mass and quantum numbers of h and H even when m_A is close to m_h or m_H, which can occur at high tanβ. CEP can therefore provide complementary information about the Higgs bosons if the MSSM is realised in nature and could allow a measurement of the $Hb\bar{b}$

coupling, which may be difficult in other production channels [1].

The $h \to b\bar{b}$ channel is one of the most challenging signals to extract using forward proton tagging. The first challenge is the Level 1 (L1) trigger strategy needed to retain the signal events, as low transverse energy jets will be heavily pre-scaled at ATLAS[2]. Detectors positioned at 420 m from the interaction point (IP) are too far away to be included in the L1 trigger decision, which has a latency of 2.5 μs. However, detectors positioned at 220 m from the IP can be included in the L1 decision. We discuss this possibility in more detail in section 7.

For events in which both protons are tagged at 420 m, which is the dominant signature for Higgs Boson masses below ~ 140 GeV, the trigger strategy could be to allow a larger L1 dijet rate, which can be significantly reduced at Level 2 (L2) by requiring two proton tags in the 420 m detectors. The reduction between L1 and L2 is approximately a factor of 20000 (140) at a luminosity of 10^{33} (10^{34}) cm^{-2}s^{-1} if both protons are detected at 420 m [16]. Furthermore, the muon-rich final state associated with b-quark decays can be exploited; approximately 10% (6%) of events can be retained by requiring a muon with transverse momentum greater than 6 (10) GeV. This muon trigger could also be employed in conjunction with a 40 GeV jet to reduce the L1 single muon rate. Finally, at low luminosity, a rapidity gap trigger could be used, requiring that LUCID, the BCM and the ZDC are devoid of activity.

The second challenge is controlling the overlap (or pile-up) background at high luminosity. The primary overlap background consists of a three-fold coincidence in one bunch crossing between an event producing a hard scatter, with the signature of interest detected in ATLAS, and two single diffractive events that produce forward protons within the acceptance of the forward detectors. The overlap background is most problematic for dijet final states because there is a large cross section for non-diffractive dijet production at the LHC[3]. For example, the overlap background to $h \to b\bar{b}$ is estimated to be a factor of 10^5 (10^7) larger than the signal for a luminosity of 10^{33} (10^{34}) cm^{-2}s^{-1}.

There are several techniques that can be employed to reject the over-

---

[1]A recent analysis has demonstrated new techniques that could provide information on the $Hb\bar{b}$ coupling if the Higgs is produced in association with a vector boson [24]

[2]Leptonic final states of sufficiently high p_T can of course be retained with the standard ATLAS trigger menu.

[3]For final states consisting of leptons, the overlap backgrounds are orders of magnitude smaller and easily dealt with by kinematic requirements on the final state.

lap background: (i) vertex matching using the dijet vertex and fast-timing detectors (discussed in Chapter 6), (ii) topological requirements, (iii) kinematic matching between the dijet system and central system measured by the forward detectors and (iv) charged track veto which discriminates against the much larger track multiplicity in non-diffractive events due to multiple parton-parton interactions. See Ref. [16] for more details. The result is that the overlap background in the $h \to b\bar{b}$ channel is negligible up to $\sim 2 \times 10^{33}$ cm^{-2}s^{-1} and smaller than the other backgrounds up to $\sim 5 \times 10^{33}$ cm^{-2}s^{-1}. At higher instantaneous luminosities, more rejection is needed (see Section 6.9 for a discussion of upgrades of the fast timing system planned to provide this additional rejection). We discuss the effects of improved overlap rejection below.

Figure 1.2 (a) shows the expected mass distribution for protons tagged at 420 m for this parameter choice given 60 fb^{-1} of data taken at 2×10^{33} cm^{-2}s^{-1}. The significance is 3.5σ. Figure 1.2 (b) shows the same distribution but for 300 fb^{-1} of data collected equally at 7.5×10^{33} cm^{-2}s^{-1} and 10^{34} cm^{-2}s^{-1} and assuming improved timing rejection (factor of 2). The significance increases to 4.5σ. The L1 trigger strategy employed is a pre-scaled jet rate trigger, allowing a L1 rate of 25kHz for 40 GeV jets[4] (which is reduced to a few Hz at L2 by requiring in-time proton hits at 420 m and basic topological requirements in the central detector), and a muon trigger $p_T^\mu > 6$ GeV.

A detailed study of the coverage in the $M_A - \tan\beta$ plane afforded by forward proton detectors at 420 m and 220 m from the interaction point was carried out in Ref. [15] for several benchmark MSSM scenarios. The event rates were calculated using an experimental efficiency based on the simulated analysis in the CMS-TOTEM studies [25], with a full simulation of the acceptance of the proposed forward proton detector system. The Level 1 trigger strategy was based on information only from the central detectors and assuming input to L1 from 220 m detectors at higher masses. Figure 1.3 shows the 3σ contours for $h \to b\bar{b}$ observation (upper plot) and $H \to b\bar{b}$ observation (lower plot). Curves are shown for 60 fb^{-1} and 600 fb^{-1}. The 60 fb^{-1} scenario was presented in Ref. [15] as 3 years of data taking at ATLAS and CMS at 10^{33} cm^{-2}s^{-1}, which was a scenario with negligible overlap background. However recent work [1,16] has shown that the overlap background is negligible up to larger luminosities, allowing ATLAS to make this measurement with 3 years of data taking at 2×10^{33} cm^{-2}s^{-1}. The

---

[4]It has been demonstrated that an additional L1 requirement that $(E_T^1 + E_T^2)/H_T > 0.9$, which could be implemented at ATLAS, would reduce this rate by a factor of two.
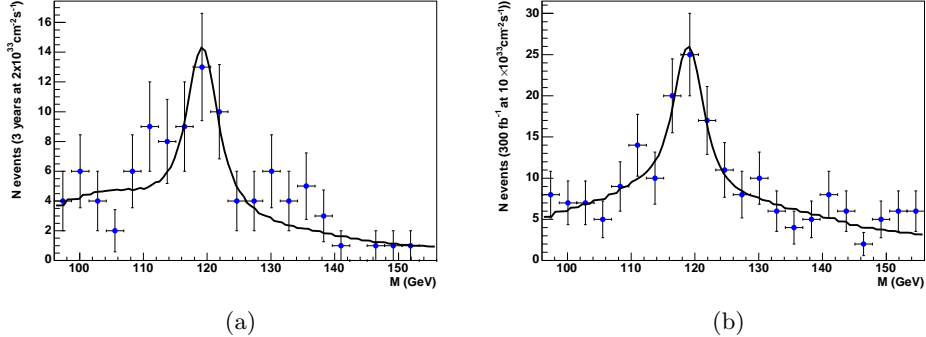
Figure 1.2: Typical mass fits for the 120 GeV/c^2 MSSM $h \to b\bar{b}$ for (a) 3 years of data taking at 2×10^{33} cm^{-2}s^{-1} (60 fb^{-1}, 3.5σ, assuming overlap rejection from a 10 ps timing system) [16] and (b) 1.5 years of data taking at 7.5×10^{33} cm^{-2}s^{-1} and 1.5 years of data taking at 10^{34} cm^{-2}s^{-1} (300 fb^{-1}, 4.5σ, assuming factor of two improvement in overlap rejection) [1].

600 fb^{-1} scenario corresponds to 3 years of data taking by both ATLAS and CMS at 10^{34} cm^{-2}s^{-1}. Figure 1.3 shows that a large region of the $M_A - \tan\beta$ can be covered at the 3σ level given enough luminosity. For example, if $\tan\beta = 40$ and $M_A = 120$ GeV/c^2, then $h \to b\bar{b}$ would be observed with 3.8σ significance with 60 fb^{-1} of data (upper plot). For $\tan\beta > 30$, the significance is 5σ or above. Such a measurement would provide a unique determination of the quantum numbers of the Higgs boson.

It is also possible to test for CP-violation in the MSSM Higgs sector. The azimuthal asymmetry in the outgoing tagged protons is expected to be quite sizable in some MSSM scenarios [11,26]. In addition, the cross sections can become so large in the MSSM that the excellent mass resolution of the forward detectors could allow a line shape analysis [7] and even make it possible to distinguish between Higgs bosons that are almost degenerate in mass, as shown for the tri-mixing scenario in Ref. [11].

In Ref. [16] it was concluded that observation of the SM Higgs boson in the $b\bar{b}$ channel will be difficult due to the small cross section and a S/B ratio less than 0.5. However, recent work [1, 27] has shown that the CEP backgrounds may be reduced resulting in a S/B>1 for data taking at instantaneous luminosities of 2×10^{33} cm^{-2}s^{-1}. Coupled with improved fast-timing resolution [1], it may be possible to observe the $h \to b\bar{b}$ channel at ATLAS. This possibility should not be ruled out without further study, as the SM
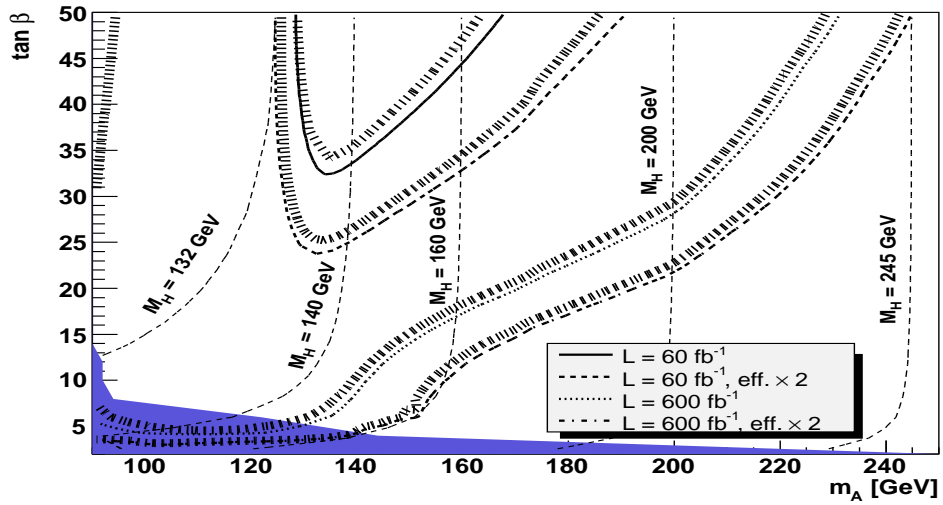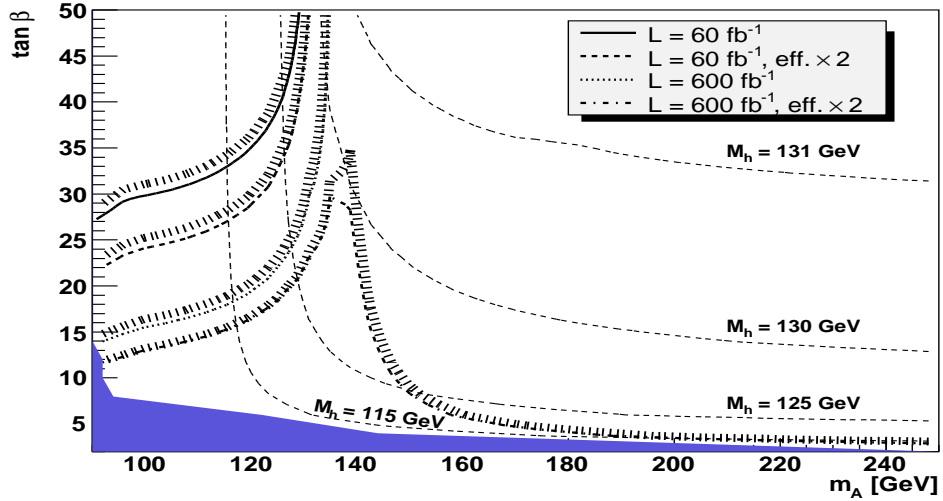
Figure 1.3: 3σ contours for $h \rightarrow b\bar{b}$ (upper plot) and $H \rightarrow b\bar{b}$ (lower plot) in the M_A - $\tan\beta$ plane of the MSSM within the M_h^{max} benchmark scenario (with $\mu = +200$GeV) for different luminosity scenarios as described in the text. The values of the mass of the Higgs bosons, m_h and M_H, are indicated by contour lines. Overlap background considered to be negligible. The dark shaded (blue) region corresponds to the parameter region that is excluded by the LEP Higgs boson searches. These plots are reprinted from Ref. [15].

9

$h b \bar{b}$ coupling and the quantum numbers of any observed state are difficult to extract at the LHC.

1.1.2 $h \rightarrow W W^*$

The cross section for central exclusive Standard Model Higgs production is approximately 3 (1) fb for a 120 (200) GeV Higgs boson [1]. The $W W^*$ channel is the simplest way to observe the SM Higgs boson in CEP because the events are easy to trigger for the semi-leptonic and fully leptonic decay modes. A study taking into account basic experimental cuts was performed in Ref. [20] assuming that forward proton detectors were operational at 220 m and 420 m from the interaction point (IP). With Level 1 trigger thresholds of $p_T > 25$ GeV/c for single electrons and $p_T > 20$ GeV/c for single muons, and reduced thresholds for dileptons, it was found that there should be approximately 3 events in 30 fb^{-1} for 140 GeV/c$^2 < M_h <$ 200 GeV/c^2. The background processes from photon-photon fusion and the W-strahlung from the CEP of light-quark dijets were studied, with the conclusion that a signal-to-background ratio of one (or better) should be achievable. For the gold-plated doubly-leptonic decay modes, there would be approximately one event per 30 fb^{-1} with no appreciable backgrounds.

It may not be necessary to impose such high leptonic trigger thresholds because forward proton detector information can be employed at higher trigger levels to reduce the rates significantly, allowing for higher Level 1 input rates. If the trigger thresholds are reduced to 15 GeV/c for both electrons and muons (which could also be achieved by demanding a coincidence with one or two jets) then the semi-leptonic signal rates double.

At high luminosity, we would expect approximately 10-20 signal events in the fully-leptonic channel in 300 fb^{-1} depending on the trigger thresholds. Note that these events have the striking characteristic of a dilepton vertex with no additional tracks allowing for excellent background suppression. In particular, the overlap background for di-lepton final states is expected to be negligible. The semi-leptonic decay channel is currently under investigation [28]. Preliminary results indicate 15-30 events in 300 fb^{-1} depending on trigger thresholds.

In the MSSM the cross section×branching ratio for CEP $h \rightarrow W W^*$ can be enhanced by up to a factor of four with respect to the SM in the so-called small α_{eff} scenario [15] for $M_h \sim$120 GeV/c^2.

1.1.3 $h \to \tau\tau$

In the MSSM, the branching ratio of the Higgs bosons to $\tau\tau$ is approximately 10% for $M_{H/A} > 150$ GeV/c^2 if the decays to light SUSY particles are not allowed. The τ's decay primarily to 1-prong (85%) or 3-prong (15%) track topologies; therefore requiring no additional tracks on the $\tau\tau$ vertex is very effective at reducing non-exclusive background.

The possibility of observing the Higgs boson through its decay to $\tau\tau$ was investigated in Ref. [15]. It was shown that the heavy neutral Higgs, H, can be observed at 3σ in this channel across a large area of the $M_A - \tan\beta$ plane; for $m_A \sim 120$ GeV, the 3σ contour extends as low as $\tan\beta \sim 10$ and at higher masses, $m_A \sim 200$ GeV, the $\tau\tau$ channel is observable for $\tan\beta > 40$. The light Higgs boson, h, can be observed at 3σ confidence for $m_A < 130$ GeV and $\tan\beta > 15$.

1.1.4 $h \to 4\tau$

The possibility of a Higgs boson decaying to 4τ arises in the NMSSM, which extends the MSSM by the inclusion of a singlet superfield, $\hat{S}$ [29]. The Higgs sector of the NMSSM contains three CP-even and two CP-odd neutral Higgs bosons, and a charged Higgs boson. According to Ref. [30] the part of parameter space that has no fine-tuning problems results in the lightest scalar Higgs boson decaying predominantly via $h \to aa$, where a is the lightest pseudo-scalar. The scalar Higgs boson has a mass of ~ 100 GeV/c^2. If the a has a mass of $2m_\tau \lesssim m_a \lesssim 2m_b$, which is preferred on general theoretical grounds, then the decay channel $h \to aa \to 4\tau$ would become the dominant decay chain. This is not excluded by LEP data and in such a scenario the LHC could fail to discover any of the Higgs bosons [30].

It was shown in Ref. [17] that the lightest Higgs boson could be discovered in CEP using forward proton detectors at ATLAS. It is expected that approximately 3-4 events will be retained (after all cuts) using a muon trigger of $p_T > 10$ GeV given three years of data taking if the instantaneous luminosity is greater than 10^{33} cm^{-2}s^{-1}. The event rates double if a combination of lepton triggers are used [1]. There is no appreciable background. The mass of the h is obtained using the missing mass method to an accuracy of 2 to 3 GeV/c^2 (per event). Furthermore, using the kinematic information provided by the forward detectors and the tracking information from the central detector, it is also possible to make measurements of the a mass; in the above scenario the mass measurement is 9.3 ± 2.3 GeV/c^2.

1.1.5 Central exclusive jet production and calibration of the ATLAS jet energy scale

It is possible to use the CEP of dijets to constrain the theoretical uncertainties associated with the CEP calculation. In addition to checking the overall normalisation, exclusive two- and three- jet production allows the study of the Sudakov suppression factor [31]. The dependence of the dijet cross section with transverse energy is steeper than would be expected on dimensional grounds, due to the Sudakov factor. The dependence of the three jet cross section on the rapidity interval spanned by the jets is also sensitive to the Sudakov effect. These measurements could be made in early data taking with ATLAS FP.

If both protons are tagged in forward detectors, a measurement of the transverse momenta and azimuthal angle of the outgoing protons allows a detailed probe of the opacity of the incoming proton and, more generally, tests the dynamics of soft-survival by studying the correlations between the outgoing protons [4, 22]. In addition, the $J_z = 0$ spin selection rule can be observed in a CEP dijet sample. As the $J_z = 0$ selection rule is applicable to all CEP processes, quark jet production is expected to be suppressed, leading to a reduced ratio of b-jets to all jets when compared to other production processes.

It is also possible to calibrate the ATLAS jet energy scale using forward proton tagging [32]. The forward proton detectors provide a precise measurement of the true parton energy if the angle of the jet is well measured. CEP jets are only affected by final state radiation, hadronisation and pile-up. It is possible therefore to measure the effects of parton showering and hadronisation in a clean environment and this could help constrain event generator models. Furthermore, the CEP of dijets can be studied at many luminosities, allowing a detailed study of the pile-up dependence of the jet energy correction.

1.2 Diffraction and QCD

Proton tagging at ATLAS will allow the study of hard diffraction, expanding and extending the investigations carried out at CERN by UA8 [33], more recently at HERA by H1 and ZEUS and at Fermilab by CDF and D0 (see e.g. [25, 34–36] and references therein). At low luminosity, single diffractive (SD) meson, dijet and vector boson production, $pp \to pX$, can be observed. At higher luminosities, double pomeron exchange, $pp \to pXp$, can be used

for similar studies, the lower event rate being compensated by additional rejection against the combinatorial overlap backgrounds (from requiring one extra proton tag and vertex matching using the fast-timing detectors). Note that DPE is distinct from CEP, as the central system contains remnants from the diffractive exchange in addition to the hard subprocess. These processes are sensitive to the low-x structure of the proton and the diffractive parton distribution functions (dPDFs). Inclusive jet and heavy quark production are mainly sensitive to the gluon component of the dPDFs, while vector boson production is sensitive to quarks. The kinematic region covered expands that explored at HERA and Tevatron, with values of β (the fractional momentum of the struck parton in the diffractive exchange) as low as 10^{-4} and of Q^2 up to tens of thousands of GeV^2.

The SD and DPE processes can also be used to determine the soft-survival probability, which is interesting in its own right because of its relationship with multiple scattering effects and hence the structure of the underlying event in hard collisions. Azimuthal correlations between the two forward protons produced in DPE allow the soft-survival factor to be probed as a function of the proton kinematics. More detailed studies, including diffractive dijet production, W and Z production and B meson production can be found in Ref. [25].

1.3   Photon-photon physics

In his section we consider elastic photon-photon collisions, $pp \rightarrow p\gamma\gamma p \rightarrow pXp$. The final state topology is similar to CEP; a central system separated on each side by a large rapidity gap from a forward proton. Photon-photon fusion opens up a rich electroweak program that complements the QCD physics present in CEP and diffraction. Furthermore, the elastic $\gamma\gamma$ effective luminosity function falls much more slowly with energy than the effective CEP luminosity function allowing larger central masses to be probed [1]. Recently, exclusive two-photon production of lepton pairs has been observed by the CDF collaboration [37] and is in good agreement with the theoretical predictions.

1.3.1   Lepton pair production

Two-photon exclusive production of muon pairs has a well known QED cross section, including very small hadronic corrections [38]. Thanks to its distinct signature, the selection procedure is very simple: two muons within

the central detector acceptance ($|\eta| < 2.5$), with transverse momenta above, for example, 10 GeV/c. After applying this selection criteria and requiring one forward proton tag, the cross section is 1.3 pb [1,39]. This corresponds to ~ 50 muon pairs detected in a 12 hour run at a mean luminosity of 10^{33} cm^{-2}s^{-1}, which is more than sufficient to calibrate the 420 m detectors to the required accuracy. More details of the calibration strategy are given in section 2.5.1.

The large event rate coupled with a small theoretical uncertainty makes this process a perfect candidate for the measurement of the absolute LHC luminosity [40]. e^+e^- production can also be studied at ATLAS, although the trigger thresholds will be larger and hence the final event rate reduced.

1.3.2 Vector boson production

The cross section of exclusive two-photon production of W boson pairs is expected to be about 100 fb at the LHC [39]. The majority of such events will have one proton tagged at 220 m and one proton tagged at 420 m due to the relatively large mass of the central system. The acceptance of the combined 220 m/420 m system as a function of mass is discussed in more detail in section 2.2.

Easiest to observe experimentally are the fully leptonic decay channels; requiring no additional tracks on the $l^+ l^-$ vertex, large lepton acoplanarity and large missing transverse momentum strongly reduces the backgrounds, such as $\gamma\gamma \to \tau^+\tau^-$. The cross section for events where both W bosons decay into a muon with $p_T > 10$ GeV and a neutrino is 0.67 (0.42) fb if one (two) protons are tagged in a forward detector at either 220 m or 420 m. For 30 fb^{-1} collected at low luminosity, one would expect approximately 20 events with one proton tag and two muons with $p_T > 10$ GeV. The double proton tag requirement is necessary at high luminosity in order to efficiently suppress the overlap background from inclusive (partonic) WW production. Thus for 100 fb^{-1}, one would expect 42 events with two proton tags. A similar study can be performed for events in which both W bosons decay to an electron and a neutrino, albeit with a reduced efficiency.

It is possible to investigate the higher rate semi-leptonic decay channel, although further studies are required to determine the effect of the overlap background. It was shown in Ref. [42] that the production cross section has a sharp turn on at $\sim 2m_W$, which allows an *in situ* calibration of the absolute forward detector energy scale to much better than 1% given 100 fb^{-1} of data. This process is also an interesting probe of the $WW\gamma$ vertex. The

coupling enters the cross section calculation to the fourth power and so should be extracted with less than 1% uncertainty given 100 fb^{-1} of data. This constraint is competitive with the standard measurement from non-diffractive $W\gamma$ production and is insensitive to many of the systematics involved in that case.

Vector boson pair production also provides an opportunity to investigate anomalous gauge boson couplings, in particular the anomalous quartic gauge couplings (QGCs) $\gamma\gamma VV$. Note that in the SM, the tree level pair production of Z bosons by photon-photon fusion is not allowed and any observation of exclusive ZZ final states implies an anomalous coupling. Conversely, the SM does allow both triple and quartic gauge couplings, $\gamma W^+ W^-$ and $\gamma\gamma W^+ W^-$ and the anomalous contribution would exist as an excess over the SM prediction.

The sensitivity of AFP to anomalous gauge couplings has been investigated in Ref. [1, 39] for the subprocesses $\gamma\gamma \to W^+ W^- \to l^+ l^- \nu_l \bar{\nu}_l$ and $\gamma\gamma \to ZZ \to l^+ l^- j\, j$, using the signature of two leptons (e or μ) with $|\eta| < 2.5$ and $p_T > 10$ GeV/c and at least one proton tagged in a forward detector. The results are presented as a 95% confidence level upper limit on the anomalous couplings given just 10 fb^{-1} of data. The limits are about 10000 times better than the best limits established at LEP2 [43], clearly showing the large and unique potential of such studies at the LHC.

1.3.3 Supersymmetric particle production

Exclusive two-photon production of new charged particles provides a simple mechanism for the production of new physics beyond the Standard Model. Two photon production of SUSY leptons has been investigated [45–48] and the cross section for $\gamma\gamma \to \tilde{l}^+ \tilde{l}^-$ can be as large as 1 fb, while remaining consistent with the direct search limits from LEP [49,50]. The production via $\gamma\gamma$ fusion has the added advantage over standard LHC production mechanisms of being a direct QED process, with minimal theoretical uncertainties.

In Ref. [44], the two-photon production of charged SUSY pairs is investigated for three benchmark points in mSUGRA/CMSSM parameter space constrained by WMAP results [51]. The two-photon production of $\tilde{e}^+ \tilde{e}^-$, $\tilde{\mu}^+ \tilde{\mu}^-$, $\tilde{\tau}^+ \tilde{\tau}^-$ and charginos (χ_1, χ_2) in the fully leptonic decay channels are considered, which means that the final state consists of two leptons and a large amount of missing energy carried by the LSP and, in the case of $\tilde{\tau}/\chi$ pair production, neutrinos. Depending on the benchmark point, about 50 signal events with S/B$\sim$ 2 in 100 fb^{-1} are expected. Results for the LM1
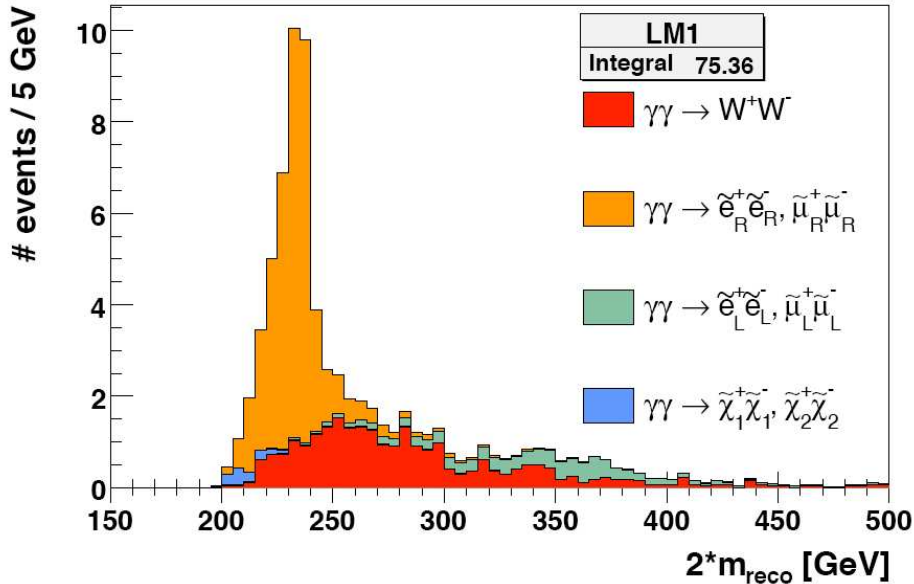
Figure 1.4: Distribution of the reconstructed mass for the LM1 SUSY signal and the WW background for an integrated luminosity of 100 fb^{-1}. Figure taken from [44]

SUSY point are shown in Fig. 1.4.

1.4 Other photon-induced processes

The two dominant subprocesses for studying top physics in photoproduction are pair production, $\gamma g \rightarrow t\bar{t}$, and associated single-top production, $\gamma b \rightarrow Wt$. The overall photo-production of top is sensitive to the as yet unmeasured top quark electrical charge. The associated single-top production is sensitive to the CKM matrix element $|V_{tb}|$. In Ref. [1], the measurement of associated single top production was investigated using a generic fast detector simulation. Two final states were considered: (i) semileptonic decay of the two W bosons, $lbjj$ and (ii) the fully leptonic decay, llb. The backgrounds considered were photoproduction of $t\bar{t}$ (with an unidentified jet), $Wjjj$ and WWq'. Cut criteria were applied, requiring the correct number of jets (with $p_T > 20$ GeV) and leptons (with $p_T > 10$ GeV) within the

16

acceptance of the detector and a forward gap or tagged proton. The single top cross section is then approximately 40 fb and the combined background is ~60 fb, implying an easy observation of this process within 1 fb^{-1} of data.

It is also possible to search for the 'exclusive' photoproduction of single top, $\gamma q \to t$, which is only allowed in the SM for higher order electroweak interactions because neutral currents preserve quark flavour at tree level. A large number of single top events would therefore indicate physics beyond the SM. The current best limit on the anomalous coupling γut is 0.14 and no limit has been set on the anomalous γct coupling. With 1 fb^{-1} of data, ATLAS FP will allow limits to be set at 0.036 and 0.062 respectively [1].

Associated WH photoproduction allows the measurement of the WWH gauge coupling and, with enough integrated luminosity, may provide information on the $Hb\bar{b}$ coupling, which is particularly difficult to extract at the LHC. The cross section for $pp \to pWHY$ is 23 (18) fb for a 115 (170) GeV SM Higgs boson [1]. Although the cross sections are small, the S/B ratio is an order of magnitude better than the quark initiated processes. Further studies are necessary to determine the luminosity required to extract the couplings.

1.5   Summary

Forward proton tagging at ATLAS has the potential to significantly increase the physics reach of the experiment. The key experimental channels only accessible with high precision using forward detectors are central exclusive production, double pomeron exchange and photon-photon physics. Two proton tags coupled with time-of-flight information from the forward detectors should allow inclusive (parton-parton) backgrounds to be adequately rejected, even for the fully hadronic final states, at high luminosity running.

CEP allows for the study of Higgs bosons in the both the Standard Model and the supersymmetric extensions, MSSM and NMSSM. For any resonance production in CEP, the quantum numbers of the produced particle are restricted to $J^{PC} = 0^{++}$ to a very good approximation. In addition, forward detectors provide an excellent mass measurement regardless of the decay products of the produced particle. CEP of jets allow the components of the theoretical calculations to be constrained and can provide parton level information for use in jet energy calibration.

Double pomeron exchange allows study of diffractive parton distribution functions and the soft-survival factor, which is responsible for the factoriza-

tion breaking observed in hard diffractive interactions between ep and $p\bar{p}$ colliders. Event rates for vector meson, dijet and vector boson production are very large.

Photon-photon physics allows absolute luminosity determination and *in situ* forward detector calibration through the well-known QED process, $\gamma\gamma \rightarrow \mu^+\mu^-$. Vector boson production in this channel allows competitive limits to be set on the anomalous quartic gauge couplings. Charged SUSY pair production could be measured for light SUSY particles and the information provided by the forward detectors will improve the mass measurement of the new particles.

In addition to these processes, it is also possible to measure single diffraction and photoproduction, in which one proton remains intact and is tagged by a forward detector. The majority of these searches have a large cross section and could be investigated during special runs. Further work is required to determine up to which luminosity the measurements can be made. Single diffraction provides additional information on the dPDFs and soft-survival by measuring meson, dijet and vector boson production. Photoproduction allows the study of single top production, allowing limits to be set on the anomalous γut and γct couplings.

Chapter 2

Acceptance, Resolution and Calibration of Forward Detectors at ATLAS

2.1 Introduction

The configuration of the LHC beamline in the ATLAS region is shown schematically in Fig. 2.1. The proposed forward detector stations are to be installed in the regions located at approximately 220 m and 420 m from the IP1 interaction point in both beamlines downstream of the central detector. In these two regions protons that have lost momentum in the collision emerge sufficiently far from the beam envelope to be detected. The acceptance and the ultimate achievable experimental resolution of the forward detectors depend primarily on the LHC beam optics and on the position of the detectors relative to the beam.

The FP420 Collaboration developed two independent programs to track protons through the LHC lattice, FPTrack [52] and HECTOR [41]. While the results in this document were obtained with FPTrack, the programs were shown to be in good agreement with each other and with the MAD-X tracking code in [1]. FPTrack implements a complete model of the LHC optics including all apertures and collimators. The largest losses of protons occur in the Main Bending dipoles. Version 6.500 of the LHC optics files is used with: $\beta^* = 0.55$ m; angular divergence $\sigma_\theta = 30.2$ μrad at the IP; crossing angle = 142.5 μrad in the vertical plane at IP1; beam energy spread $\sigma_E = 0.77$ GeV. The beam energy spread is the largest irreducible limit-
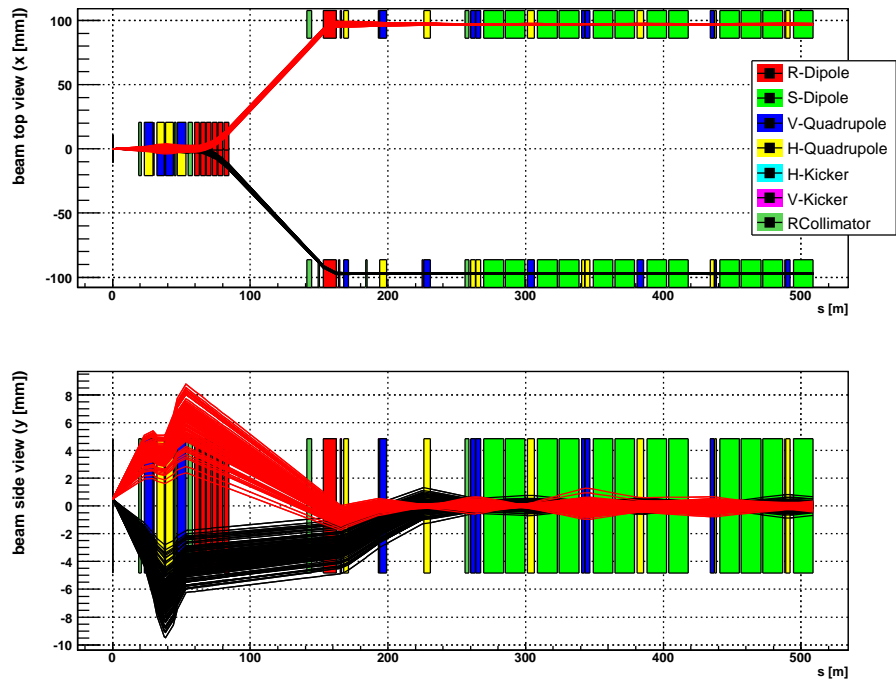
Figure 2.1: Schematic plan view and side view of the beamline at IP1 (AT-LAS). The horizontal curvature of the beamline has been neglected out for presentational purposes.

ing factor on the mass resolution obtainable using forward proton tagging detectors at the LHC.

Unless otherwise stated, we use the ExHuME Monte Carlo [53] to generate outgoing protons from the central exclusive production of a SM Higgs boson, although the results apply for any centrally-produced system of the same mass. We show acceptances below for both 420 m alone and for 420 m and 220 m stations operating together.

2.2 Detector acceptance

The position and direction of a proton in the 220 m and 420 m detectors (for a given LHC optics) depend on the energy loss and scattering angle of the outgoing proton and the z-vertex position of the collision. The energy loss and scattering angle are directly related to the kinematic variables ξ, the fractional longitudinal momentum loss of the outgoing proton, and $-t$, the square of the four-momentum transfer at the proton vertex. A measurement of the position and angle of a proton track at 220 m and 420 m relative to the beam and the z-vertex position of the collision enables the energy loss and angle of the protons at the IP to be reconstructed. The transformation is highly non-linear owing to the energy dependence of the transfer matrices.

The low-ξ (and therefore low-mass) acceptance depends critically on the distance of approach of the active area of the silicon sensors from the beam. This is shown in Fig. 2.2 for proton tags at 420 + 420 m and 420 + 220 m. Operating as far away as 7.5 mm does not compromise the acceptance for central masses of 120 GeV and above, for 420 + 420 m tagged events. Acceptance at higher masses requires the 420 m detectors to be used in conjunction with 220 m detectors. In Fig. 2.2 (right) the acceptance is shown for varying distances from the beam of the 220 m detectors, with the 420 m detector position fixed at 5 mm. The acceptance is very sensitive to the distance of approach of the 220 m detector for masses in the 120 GeV range. For central masses above $\sim$ 140 GeV, the use of 220 m detectors becomes increasingly important.

Figure 2.3 shows several interesting features of the acceptance, including differences between the IP1 (ATLAS) and IP5 (CMS) regions. The upper plots show that if the 220 m detectors are sufficiently far from the beam (3 mm in this case) then there is negligible difference in the 420 m +420 m acceptance between IP1 and IP5, and beam 1 and beam 2. The fact that
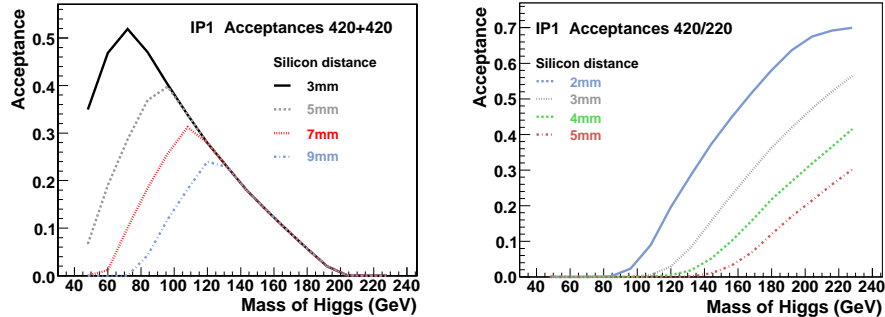
Figure 2.2: Acceptance as a function of centrally produced mass for (left) 420 + 420 m proton tags for the silicon detector active edge positioned at different distances from the beam; (right) for 220 + 420 m proton tags with the 420 m silicon at 5 mm from the beam and the 220 m at different distances from the beam. The small upward deviation at high mass for the 2 mm silicon positions shows the additional acceptance from 220 + 220 m coincidences.

the crossing angle is in the vertical plane at IP1 and the horizontal plane at IP5, however, results in a higher acceptance at IP1 than IP5 for 420 + 220 m events. The bottom plots show that for closer insertions at 220 m (2 mm in this case), there is a decrease in the 420 m + 420 m acceptance for the IP1 region, due to the dead region (from the thin vacuum window) of the 220 m detectors intercepting protons that would otherwise be detected at 420 m. This dead region is taken to be 0.7 mm in this figure. The effect is negligible for 220 m detector positions in excess of 2 mm from the beam line. The accuracy of the proton momentum measurement is higher at 420 m than at 220 m, so the operating conditions at 220 m must be chosen so as to achieve an optimum balance between the mass resolution and acceptance.

2.3 Resolutions

Typical $x-y$ distributions of hits in a detector at 420 m are shown in Fig. 2.4. Polynomial-based parametrization formulae have been developed in order to evaluate the proton momenta from the measured track position and angle in the silicon detectors. The formulae are based on fits to the track positions and angles, using generated values of the momentum and emission angle at
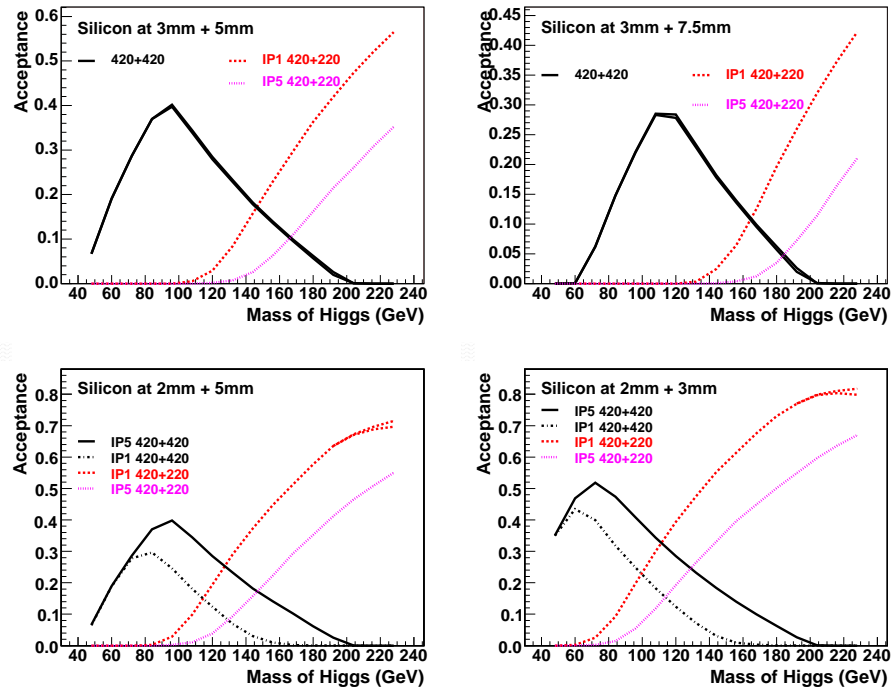
Figure 2.3: Acceptances as a function of Higgs boson mass with detector active edge at various distances from the beam centre at 420 m for IP1 (dotted line) and IP5 (dashed line). Also shown is the acceptance for events with one proton detected at 220 m and one proton at 420 m (or also 220 m, upper branch). The smaller distance in the legend is always the 220 m distance.

the IP, and averaging over the width of the beam-beam interaction region. It is found that an angular measurement in the horizontal plane θ_x is required to give good momentum reconstruction accuracy. This measurement must be particularly precise at 420 m. A precision of ± 1 μrad is necessary and attainable (see Section 5.7); the track positions must be measured over an 8 m lever arm with better than 80 μm precision at the front and back of the detector station.
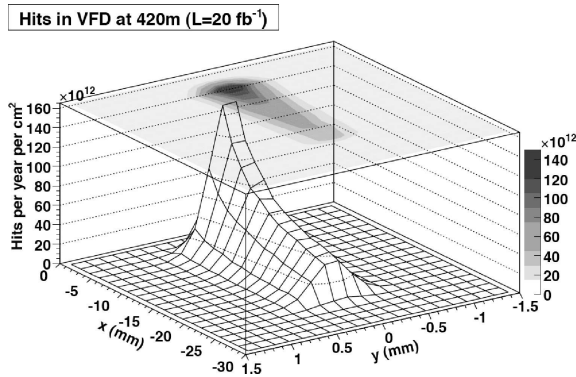

Figure 2.4: Number of proton hits due to the process pp $\to$ pX for 20 fb^{-1} integrated luminosity. Protons were generated with PYTHIA 6.2.10 (single diffraction process 93) and emerge here in the $-x$ direction.

From the momentum loss of both protons in an event, the mass of the centrally produced system can be calculated by a missing-mass formula [1]. Using the above parametrizations we evaluate the resolution achievable on the missing mass of a centrally produced object. We present results for a vertex at $z = 0$; the dependence on the z vertex within the interaction region is found to be small. We note that z will be well measured by the central detector for every event, so that offline corrections may be easily applied.

The following factors affect the mass resolution of a particle produced in the exclusive double diffraction process:

- The Gaussian width of the momentum distribution of the circulating proton beam. This is 0.77 GeV.

- The lateral uncertainty of the position of the interaction point. This is taken to be 11.8 μm from the intrinsic beam width, but could be improved if the central silicon detector system provides a better measurement on an event-by-event basis.

24

- The position measurement uncertainty in the detector system

- The angular measurement uncertainty in the detector system.
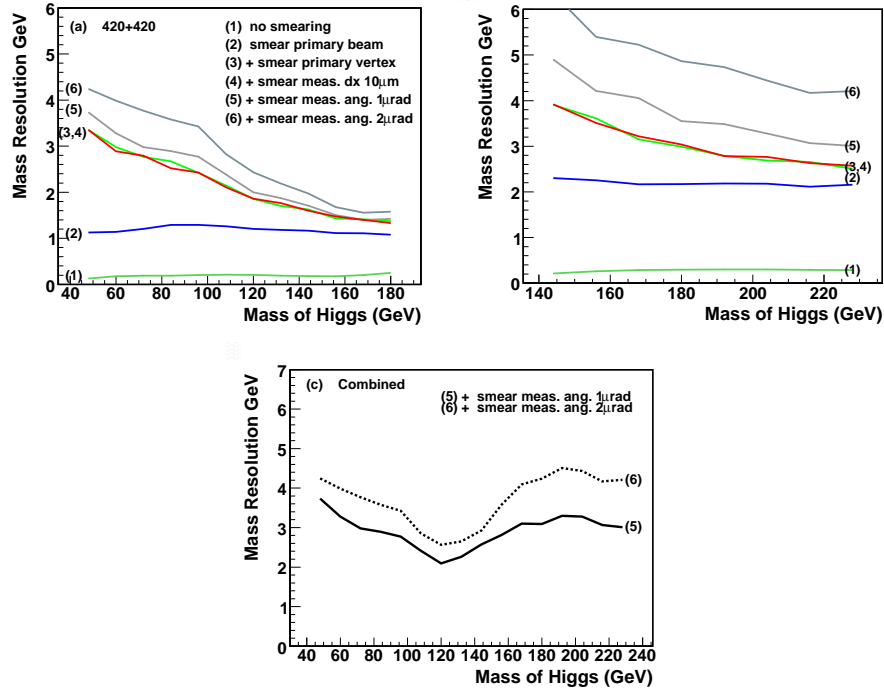
Figure 2.5: Mass resolutions obtainable in ATLAS (a) for 420 + 420 m measurements, (b) for 420 + 220 m measurements, (c) combined. The curves have different amounts of smearing applied as explained in the text.

Figure 2.5 shows the effect of the above factors on the mass resolution. Figure 2.5 (a) shows the mass resolutions for 420 m + 420 m and Fig. 2.5 (b) shows 420 m+220 m mass resolutions. Resolutions are determined by applying Gaussian smearings and fitting the resulting histograms of reconstructed minus true mass with a Gaussian, whose width is plotted here. The sets of curves represent the resolutions obtained: (1) with no physical smearing applied, indicating the precision of the reconstruction algorithm, (2) applying smearing due to the 0.77 GeV Gaussian distribution of the primary proton beam momentum (3), also including a 10 μm lateral smearing of the interaction vertex within incident beam spot, (4) also including a 10 μm smearing

of the measured position x in the silicon system, (5,6) also including 1, 2 μrad smearing, respectively, of the dx/dz measurement in the silicon system. The curves in Fig. 2.5 (c) give the combined resolutions for 420 m + 420 m and 420 m + 220 m. The effects of smearing of the x measurement (that is, the lateral displacement of the proton track from the beam) in the silicon system are seen to be small in comparison with the other effects. The overall resolution is between 3.5 GeV and 2 GeV in the mass range of interest for 420 m + 420 m tags, using the expected 1μrad angular uncertainty in the dx/dz measurement, and $\sim$ 4GeV for 420 m +220 m tags. The 2 μrad curve may be considered an upper limit to the resolution, as a comparable resolution can be obtained by simply constraining the angle of the emitted proton to be along the beam direction at the interaction point (effectively assuming that $|t| = 0$ GeV^2, which is a reasonable approximation for CEP and $\gamma\gamma$ events.)

It is possible to determine the transverse momentum of the proton as it emerges from the interaction point, again by means of polynomial-based parametrization formulae using the measurements in the detector stations. Both x and y measurements are required for this. The measurement is degraded by two factors. The angular beam spread at the interaction points is equivalent to a $\pm$ 0.21 GeV/c transverse momentum spread, both horizontally and vertically, and the poorer measurement uncertainty in the y direction increases the overall uncertainty on p_T significantly. Studies are continuing to determine the requirements for particular physics studies and whether they can be achieved.

2.4 Alignment

The reconstruction of the proton momentum depends in principle only on the optics of the two beamlines, the nominal values of which have been used in the calculations presented above, and the position of the silicon sensors relative to the beam. In practice, however, the magnet currents will vary from fill to fill, and the fields in the magnets will vary accordingly. It will therefore certainly be the case that the nominal formulae will not hold precisely. The FP420 collaboration has considered two independent alignment strategies. One is to use a high-rate physics process detectable in the ATLAS central detector which produces proton tracks in the detectors of known energy. This strategy is independent of the precise knowledge of the LHC optics between the IP and the detectors. We describe this in detail

in Section 2.5. It will also be necessary to have a real-time alignment system to fix the position of the detectors relative to the beam and provide complementary information to the off-line calibration using tracks. An independent real-time alignment system is also essential for safety purposes while moving the detectors into their working positions. Two options, both based on Beam Position Monitors (BPMs), are being considered: a 'local' system consisting of a large-aperture BPM mounted directly on the moving beampipe and related to the position of the silicon detectors by knowledge of the mechanical structure of the assembly, and an 'overall' system consisting of BPMs mounted on the (fixed) LHC beampipe at the two ends of the system, with their positions and the moving silicon detectors' positions referenced to an alignment wire using a Wire Positioning Sensor (WPS) system. Figure 2.6 shows schematically the proposed 'overall' alignment subsystem. To simplify the illustration only one moving beam pipe section is shown. The larger aperture BPMs for the 'local' alignment system are not shown (one would be mounted on each moving beam pipe section). It is likely that both the local and overall BPM alignment schemes will be implemented.
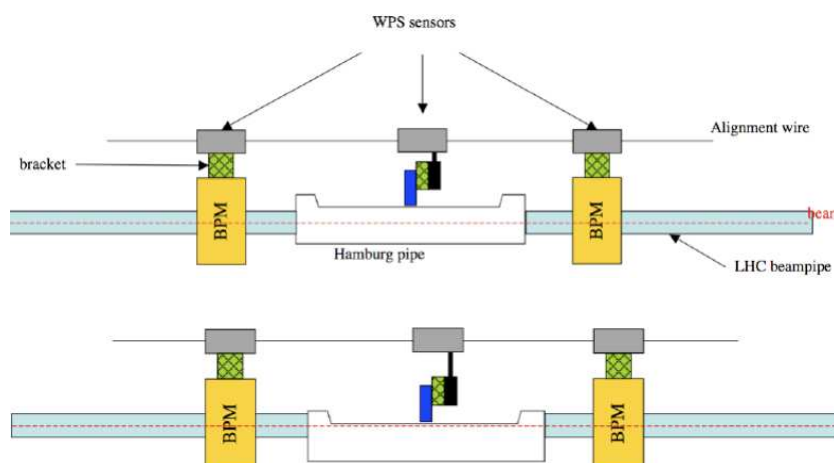

Figure 2.6: The proposed overall alignment system, shown with detectors in garage position (top picture) and in operating position (bottom picture).

Sources of uncertainty in such a system include the intrinsic resolution of the WPS system, the intrinsic resolution (and calibration) of the BPMs, and the mechanical tolerances between the components. The mechanical

uncertainties may be affected by temperature fluctuations and vibrations in the LHC tunnel, and the movement of the detectors relative to the beam must be taken into account. The individual components of the system, with comments on their expected accuracy, are described in the following sections.

2.4.1 Beam position monitors

A direct measurement of the beam position at the detector positions can be obtained with beam position monitors (BPMs). Although there are several pickup techniques available, an obvious choice would be the type used in large numbers in the LHC accelerator itself. The precision and accuracy of these electrostatic button pickups can be optimized through the choice of electrode geometry and readout electronics. While BPMs can be made with precision geometry, an important issue is balancing the gain of the right and left (or up and down) electronics; one can have a time-duplexed system such that the signals from opposing electrodes are sent through the same path on a time-shared basis, thus cancelling any gain differences. Multiplexing of the readout chain will avoid systematic errors due to different electrical parameters when using separate channels and detuning through time and temperature drift. Preliminary tests with electrostatic BPMs designed for the CLIC injection line have shown promising behavior on the test bench, even when read out with general purpose test equipment. More details can be found in Ref. [1].

Although the requirements are not as demanding for the LHC as for AT-LAS FP, it is our expectation that the necessary level of precision, resolution and acquisition speed can be obtained. It should be emphasized that the precision will depend to a large extent on the mechanical tolerances which can be achieved. Tests of these BPMs are underway on an alignment bench. Several strategies and optimizations have been proposed to reach precision and resolution of a few microns, and to achieve bunch-by-bunch measurement. The effect of the intrinsic non-linearity of button electrodes can be reduced if the particle beam passes close to the center of the pickup in the operating position. In the case where only two electrodes are required, the linearity of the signal can possibly be further improved by larger electrodes. While the detectors are in the parking position, away from the beam, the beam position measurement is also less critical. Wide band amplifiers are a possibility to obtain single shot measurements whereas narrow band amplifiers should allow a better resolution and signal-to-noise ratio.

Multi-turn integration will improve the resolution at least by a factor

10. Bunch/bunch measurements will still be possible since the bunches in LHC can be tagged, allowing measurements of each bunch to be integrated over a number of turns. The variation of one specific bunch between turns is expected to be small.

Shortly before the installation of each complete ATLAS FP section (with trackers and BPMs) a test-bench survey using a pulsed wire to simulate the LHC beam will provide an initial calibration of the BPMs. Further in-situ calibration can be done by moving each BPM in turn and comparing its measured beam position with that expected from the measurements in the other BPMs in the system; the potential for success of such an online BPM calibration scheme has been demonstrated with cavity-style BPMs intended for use in linear colliders [57, 58]. Such calibration may even be possible at the beginning and end of data-taking runs when the BPMs are being moved between garage and operating positions, removing a need for dedicated calibration runs.

2.4.2   Wire positioning sensors

Wire Positioning Sensor (WPS) systems use a capacitive measurement technique to measure the sensors' positions, along two perpendicular axes, relative to a carbon-fibre alignment wire. Such systems have been shown to have sub-micron resolution capability in accelerator alignment applications and will be used in LHC alignment. The principle of operation is shown in Fig. 2.7. Photographs of a sensor (with cover removed) and of two end-to-end sensors are shown in Fig. 2.8.
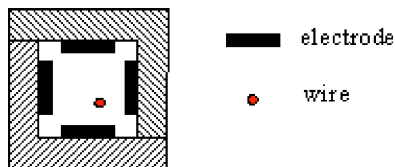

Figure 2.7: A cross-sectional schematic of a WPS sensor and alignment wire.

2.4.3   The moving detectors

The silicon detectors will be mounted on moving beampipes. The detectors however must be referenced to the fixed WPS sensors. One way to achieve
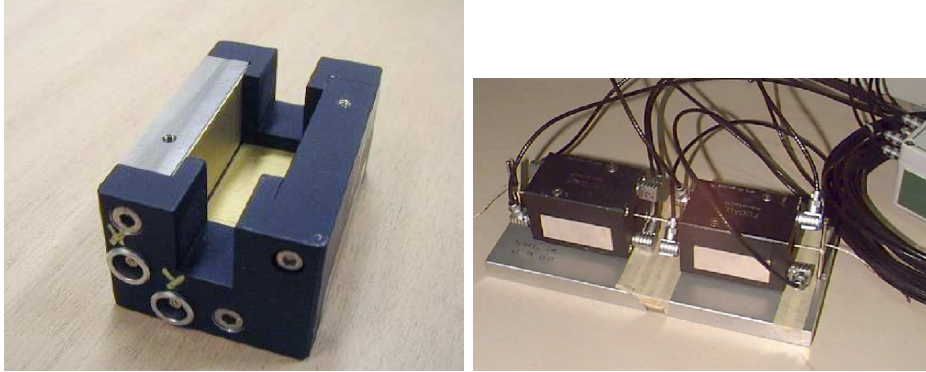
Figure 2.8: A WPS sensor with lid removed (left), showing the electrodes. The aperture is 1cm square. Also shown are two WPS sensors on the test bench (right).

this is to use an LVDT or similar mechanical displacement-measurement device. Unfortunately, "off-the-shelf" examples with long enough stroke length to accommodate the motion of the moving beampipe tend not to have sufficient accuracy, and they (particularly their readout electronics) are not generally guaranteed to be radiation-hard at the level needed by FP420. However, Schaevitz® have made special LVDTs for aligning the LHC collimators [59]. These devices are by design sufficiently radiation-hard for our purposes, and although they are longer and less accurate than required for ATLAS FP, initial discussions with the company have resulted in the expectation that a similar device to meet ATLAS FP's needs can be manufactured; currently prototypes are being designed. In the event that this fails, there are potential fallback solutions, including a combination of a long stroke-length LVDT for the garage position with a shorter, more accurate device for the operating system; or an optical positioning (e.g. laser-based) system.

2.5   Momentum calibration using tracks

The spectrometer performance can be degraded by small misalignments of the LHC elements, in particular the quadrupoles. It is found that quadrupole misalignments of the order of 0.1 mm can move the peak position of a Higgs-like signal at 115 GeV by approximately 1.4 GeV per misaligned quadrupole [41], and such effects will combine in quadrature. A partial correction can be

applied using BPM information, but a calibration method based on tracks of known momentum passing through the detectors is highly desirable.

2.5.1   Calibration using lepton pairs

The production of exclusive dileptons, $p + p \rightarrow p + e^+e^- + p$ and $p + p \rightarrow p + \mu^+\mu^- + p$ gives a near ideal calibration of the forward systems at 420 m. Measurement of the rapidity and invariant mass of the central dilepton system allows for both forward proton momenta to be calculated with very high precision. It is not necessary to detect both protons in the forward detectors, since each outgoing proton momentum loss is known under the assumption that the p_T of the outgoing protons is zero. The $\mu^+\mu^-$ process is easier to trigger on and will have less background. There are two contributing processes. Two photon production $\gamma\gamma \rightarrow \mu^+\mu^-$ is a purely QED reaction with a precisely known cross section, and as such has been proposed as a means of calibrating the LHC luminosity. The dimuon mass $M(\mu^+\mu^-)$ is a continuum. The other important process is diffractive vector meson V photoproduction: $\gamma p \rightarrow \Upsilon p \rightarrow \mu^+\mu^- p$. The Υ photoproduction cross section ($\times$ branching ratio) is larger in the mass range 9 to 11 GeV/c^2 than the two-photon continuum, so a trigger that includes this region is desirable, and achievable.

At 420 m protons with energy loss as low as 20 GeV, $\xi = 0.0029$ are accepted. For an exclusive muon pair with energies E_1, E_2 and longitudinal momenta p_{z1}, p_{z2} the energy loss $\Delta p_{1,2} = \frac{1}{2}(E_1 + E_2 \pm p_{z1} \mp z_2)$. The exclusive events can be selected in the presence of pile-up, by requiring no other tracks on the dimuon vertex, and $\Delta\phi_{\mu\mu} \approx \pi$ with $p_T(\mu^+) \approx p_T(\mu^-)$, or $p_T(\mu^+\mu^-) \leq 1$ GeV/c, with a consistent track in the 420 m tagging system. The dominant uncertainty of the forward proton momentum comes from the incoming beam spread. Figure 2.9 shows the rates of tagging muon pairs in ATLAS assuming a trigger threshold of 6 GeV for the p_T of the muons. If this could be reduced to 4 GeV, the rates would approximately double. Depending on the luminosity, accumulating a few hundred events to apply this calibration method might take several days. However, the rates achievable at 220 m, assuming a reasonable distance of the silicon from the beam, are too small for this method to be useful.

A reaction that could provide information to calibrate the forward detectors at 220 m is the bremsstrahlung process $p + p \rightarrow p + p + \gamma$ with the photons emitted into a very forward cone. The cross section is ~ 10 nb for $E_\gamma > 100$ GeV. The photon may be detected in the ATLAS Zero De-
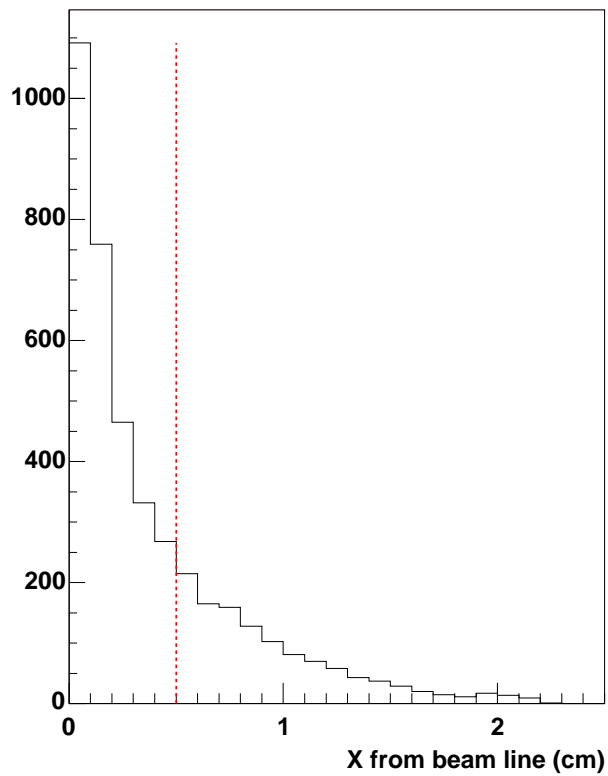
Figure 2.9: Rates per mm from the beam centre for protons detected in the 420 m silicon system corresponding to 1 fb^{-1} integrated luminosity with a dimuon pair in the ATLAS central detector with $p_T > 6$ GeV. The red line indicates a possible location of the inside edge of the silicon detector at 5 mm from the beam.

gree Calorimeter, ZDC, at 140 m. By recording coincidences between ZDC signals and protons in the 220 m tagger, a calibration of the latter can be achieved. Rates are in principle high, e.g. 20 m events per tagger per fb^{-1} over a photon energy range of 100-500 GeV. The ZDC will itself require calibration, which could be done using the same process in a well-calibrated 420 m system if a suitably scaled down trigger can be implemented. Continuum backgrounds from π^0 detected in the ZDC will be present, but can be parametrized and subtracted. The angular distribution of bremsstrahlung photons is very forward peaked which helps with background reduction *and* can be used to monitor the beam direction (tilt) at the IP.

A further possibility for cross-calibration is to use the subset of protons that pass through both the 220 m and 420 m detector systems. Since there is multiple scattering in the 220 m system, the trajectory of the proton at 420 m must have a cut placed on its apparent angle of emergence at the interaction point, and only the central section of the distribution will be usable for calibration purposes. A loss factor of up to 5 could be generated here, but the rates are high provided that the 220 m silicon can be operated sufficiently close to the beamline to intersect the trajectories of the 420 m detectable protons.

2.6   Alignment of 220 m detectors

At 220 m the rate for dimuon production is insufficient for a calibration to be performed on a fill-by-fill basis. Cross calibration using events with one proton at 420 m and one proton at 220 m, and a central system measured in ATLAS, is being investigated. The highest rate process will be exclusive dijet production. Preliminary studies suggest that a calibration of the 220 m detectors at the 5 GeV level will be possible using these events on a fill-by-fill basis. BPM-based calibration will be carried out as for the 420 m detectors.

It is possible that elastic events could provide a calibration of the 220 m detectors independent of 420 m. At the 220 m location, the beam is squeezed in the horizontal direction with a half-width of $\sigma_x = 70$ μm for beam 1 ($\beta_x = 8.74$ at 224 m) and $\sigma_x = 80$ μm for beam 2 ($\beta_x = 12.4$ at 224 m) while being wide in the y-axis direction. Elastic events therefore form an elongated ellipse in the vertical direction.

Elastic events can be detected by the same Roman pot detector technique as used by ALFA. In this case, the detectors approach the beam in vertical direction, i.e. along the major axis of the ellipse. For Roman pot

positions at about 220 m, the elastic events with $p_T > 3$ GeV/c can be observed if the Pots are operated 8 mm away from the beam (15 times the vertical beam half width). However, the elastic cross section at these large scattering angles is not well known, with more than an order of magnitude difference between the theoretical predictions of Islam [60] and Donnachie-Landshoff [61]. Assuming a 50% efficiency for triggering and detecting elastic events, the estimated daily rate at $\mathcal{L} = 10^{33}$ cm$^{-2} \cdot$ s^{-1} is between 3 and 50 events. Simulations including beam and detector effects show that precision of about 5 μm in the detector horizontal position could be reached with 100 elastic events.

To propagate the alignment of the vertical detectors to the horizontal detectors at 220 m, soft single diffractive events with tracks in both the vertical and horizontal detector systems can be used.

The estimated event yield remains uncertain until the elastic cross section at high p_T is measured at LHC, but, in principle, elastic events could be used to cross-check the alignment of the forward proton detectors at 220 m at least on a week-by-week basis.

Further studies are required to determine whether the installation of vertical alignment pots at 220 m is necessary, practical and cost-effective. The TOTEM Roman Pot units, also used in ATLAS by ALFA [62], are suitable, and could be used without any mechanical modifications. The 48 mm width of the free space is enough to hold 8 layers of 3D silicon detectors and two layers of trigger silicon, which is sufficient for alignment purposes if the elastic rate is high enough.

2.7 Summary

In this section we have shown that detectors at 420 m can cover a central mass range of between ~ 80 and 140 GeV for double-tagged CEP and $\gamma\gamma$ processes if operated at a distance of 5 mm from the LHC beams. With the addition of 220 m detectors, central masses up to 1 TeV can be observed. Using a combination of a track-based calibration based on the $p + p \rightarrow p + \mu^+\mu^- + p$ process, and a real-time calibration using beam position monitors and a wire positioning system, the 420 m system can be calibrated to achieve a Gaussian resolution of width ~ 2.5 GeV on the mass of a 120 GeV Higgs boson (or any other central system). The 220 m stations can be cross-calibrated using 220 m/420 m events, and an calibration method using elastic events is under investigation.

Chapter 3

Installation of Detectors at 220 m and 420 m from ATLAS

The detection of CEP in the mass range ~ 120 GeV requires the installation of proton tagging detectors in the cold region of the LHC 420 m from the ATLAS IP. The FP420 Collaboration commissioned the CERN design office, working with the TS/MME group, to design a cost effective and safe replacement for the 420 m connection cryostat that will be present at LHC start-up. The design requirements were to provide warm beam pipes and sufficient space to install moveable silicon tracking and fast timing detectors with little or no disruption to the LHC itself. In this chapter, we describe the new connection cryostat design.

3.1   New connection cryostat

The LHC dispersion suppressor and arc magnets are placed in one continuous cryostat from the Q7 quadrupole downstream of an IP, all the way to the Q7 quadrupole of the next IR [55]. At the position of the missing magnet of the dispersion suppressor, some 420 m downstream of each IP, there is a 14 m long Connection Cryostat (CC) which contains cold beam-pipes, the 2K heat exchanger, or X-line, and various cryo-lines which run throughout the continuous cryostat. The CC also carries the superconducting busbars of the main bending magnets and quadrupoles and nearly 100 superconducting cables for corrector magnets and other systems. There are sixteen
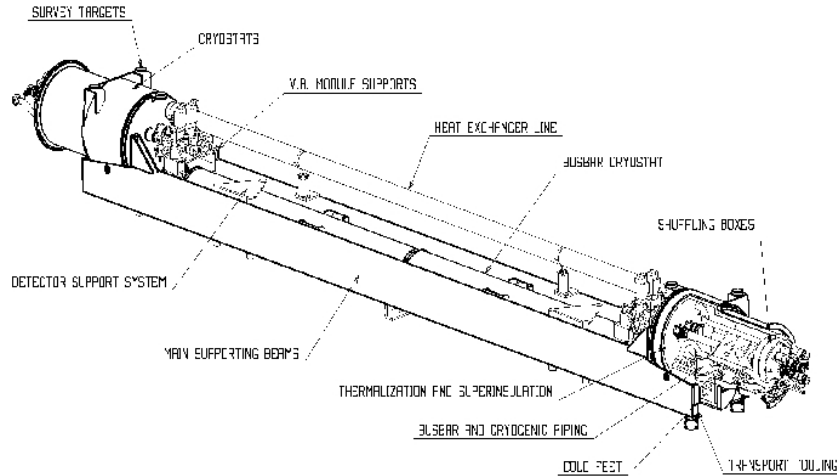
Figure 3.1: The new connection cryostat for FP420

CCs in the LHC, each made to be as similar as possible to a standard arc cryostat, at least as far as interconnection and handling are concerned. At this 420 m point, the dispersion function D, with the standard high luminosity optics, is approximately 2 m and hence protons from the IP which have lost around 1% of their momentum are well separated from the circulating beam, as described in Chapter 2. In order to allow the use of near beam detectors at this 420 m position it is proposed to replace the existing connection cryostats on each side of IP1 with a warm beam-pipe section and a cryogenic bypass. A New Connection Cryostat (NCC) with approximately 8 m of room temperature beam-pipes has been designed using a modified Arc Termination Module (ATM) at each end.

In addition to two modified ATMs and warm beam-pipes, the NCC shown in Fig. 3.1 has a small cross section cryostat below the beam-pipes carrying all the cryo-lines and superconducting circuits and a new specially designed cryostat for the X-line. All this is supported by two longitudinal beams to make a single unit which can be directly exchanged for an existing connection cryostat. The passage of the X-line through the ATM modules is the main modification needed to the standard ATMs, but the geometrical layout of this passage has been arranged to be as far away as possible from
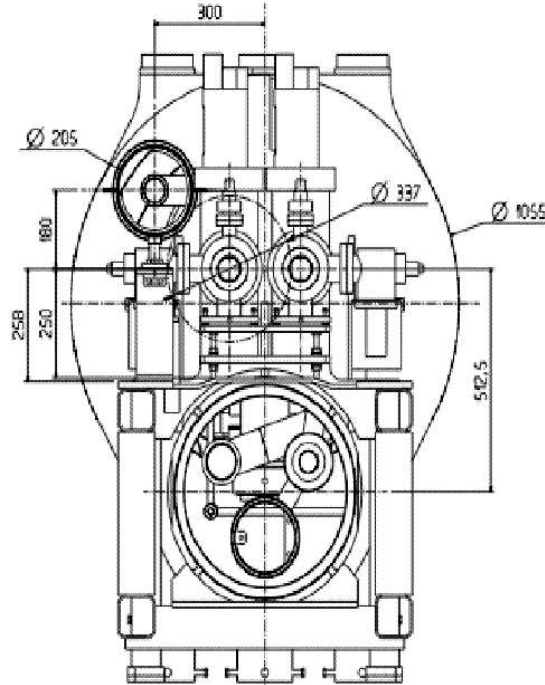
Figure 3.2: Cross-section view of the new connection cryostat for FP420

the downstream beam-pipe in order to leave adequate space for near-beam detectors and their associated equipment. The cross-section of the NCC, with the space around the beam-pipes available for detectors and associated mechanics, is shown in Fig. 3.2.

The existing connection cryostat contains a box structure of lead plates of 15 mm thickness enclosing the two beam-pipes to reduce the radiation field in the tunnel, essentially replacing the shielding provided by the cold mass in a standard arc dipole cryostat. The same thickness of lead shielding will be provided around the warm beam-pipes and detector stations of the NCC.

There are also short lengths of cylindrical shielding in the form of collars around the beam-pipes at each end of the existing connection cryostat to limit the risk of quenching adjacent superconducting magnets. Similar collars will be incorporated into the modified ATM's at each end of the NCC

in order to ensure that the NCC is at least equal to the existing cryostat in terms of influence on the local radiation fields and quench performance.

	Normal Days
Warmup from 1.9K to 4.5 K	1
Warmup from 4.5K to 300 K	15
Venting	2
Dismantling interconnection	10
Removal of the connection cryostat	2
Installation of the FP420 cryostat	5
Realization of the interconnections	15
Leak test and electrical test	4
Closing of the vacuum vessel	1
Evacuation/repump	10
Leak test	2
Pressure test	4
Cooldown from 300 K to 4.5 K	15
Cooldown from 4.5K to 1.9 K	3
Total [days]	89

Table 3.1: The estimated time in days required to install one NCC

The engineering design of the new connection cryostat is in progress in the CERN central design office of the TS/MME group. The design aim is to meet or exceed the same specifications as the existing connection cryostat, whilst providing the maximum useable space for the silicon and timing detectors at 420 m. The preliminary design offers acceptable solutions for all cryogenic and mechanical engineering aspects as well as integration into the LHC environment [63, 64]. The final cryogenic performance will depend on the detailed design, but it has already been established that the additional static heat load arising from the two additional cold to warm transitions will be tolerable for the LHC cryogenic system. During LHC operation, simulations show that the NCC actually contributes a slightly lower dynamic heat load than the existing connection cryostat, because in the 8 m long warm section some synchrotron radiation is being absorbed at room temperature.

The detailed design of this second generation connection cryostat, the NCC described above, is in progress. It would in principle be possible to

build two complete NCC's in about a year and have them tested and ready for installation at the end of 2009. Vittorio Parma of the AT Department's MCS group has accepted to take responsibility for the NCC cryostat. He is leading a working group which will verify the compatibility of the existing conceptual design and develop the detailed design for manufacture. As regards construction of the NCC's, the sixteen ATM modules of the LHC were assembled at CERN in a dedicated workshop in Building 110, under the responsibility of Ramon Folch (TS/MME). His team has already prepared a preliminary construction schedule and cost estimate for the new NCC cryostats [65].

The cutting and removal of the existing connection cryostat and its replacement by an NCC is very similar to the replacement of a standard LHC dipole and the task has been evaluated by the group responsible for all the LHC interconnections. Table 3.1 shows the sequence of operations and the estimated time needed in normal working days to complete the exchange of a connection cryostat from start of warm-up to being ready for beam. It is thus conceivable that the installation of an NCC cryostat and near-beam detectors could be completed in a standard long shutdown. A preliminary study of the transport aspects has shown that adequate tooling exists and it can be expected that the time needed will be in the shadow of other operations shown in Table 3.1. However, the number of Connection Cryostats that can be replaced in a standard annual shutdown will depend on the number of LHC magnets requiring replacement and the work load of the interconnection teams.

3.2 Installation of detectors at 220 m

We propose to install an identical detector system in the 220 m region of the LHC. There is space available for detector systems at 216 m and 224 m, giving an 8m lever arm for tracking similar to that proposed at 420 m. Because the LHC is warm at 220 m, installation is relatively trivial. The layout of the LHC in the 220 m region is shown schematically in Fig. 3.3.

3.3 Summary

In summary, a preliminary design for a replacement connection cryostat that would allow near beam detectors to be placed in the 420 m region has been completed, and a final design is in progress. The solution proposed
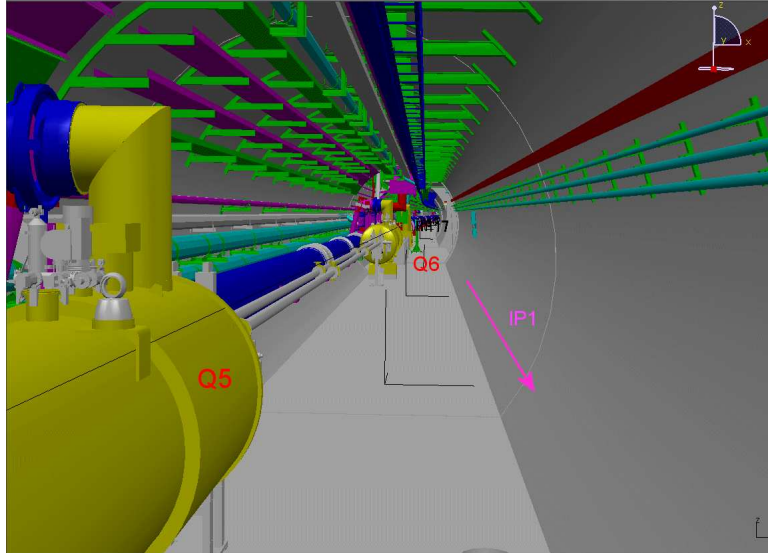
Figure 3.3: Schematic view of the LHC configuration between quadruples Q5 and Q6 (Courtesy of D. Macina).

is expected to have an acceptable cryogenic performance and give similar radiation profiles in the region. With the appropriate approvals and funding, two such cryostats could be built and ready for installation in a three-month shutdown in 2010, with negligible risk to LHC operations.

Chapter 4

Hamburg Beam-pipe

4.1 Introduction

In this chapter we describe the movable beam pipes that we propose to use to host the 3D silicon and timing detectors needed to tag and measure protons both at 220 and 420 m.

Detection of protons at 420 m from the IP requires detectors to be placed between the two LHC beam-pipes, the exteriors of which are separated by about 140 mm (the distance between the pipe axes is nominally 194 mm). In addition, the nearby cryogenic lines limit the available free space. Due to these space constraints the traditional Roman Pot (RP) technique cannot be used, and another concept for near beam detectors, pioneered at DESY [66], was proposed by FP420 [1]. At 220 m, it would be possible to use Roman pots since the detectors are placed in the warm region, but the space available to host both the silicon and timing detectors is too small if one uses the TOTEM design. Since the Hamburg pipe solution developed by FP420 can also be employed at 220 m, ATLAS FP will use it at both locations.

The moving pipe technique has many advantages with respect to the RP design. It allows much simpler access to detectors and provides direct mechanical and optical control of the actual detector positions. In addition, unlike the Roman pot case which involves forces from pressure differences as the detectors are inserted into the vacuum, the Hamburg pipe maintains a fixed vacuum volume. This results in much less mechanical stress, consequently allowing a very simple and robust design. In effect, the Hamburg Pipe is an instrumented collimator, and the LHC collimator control system
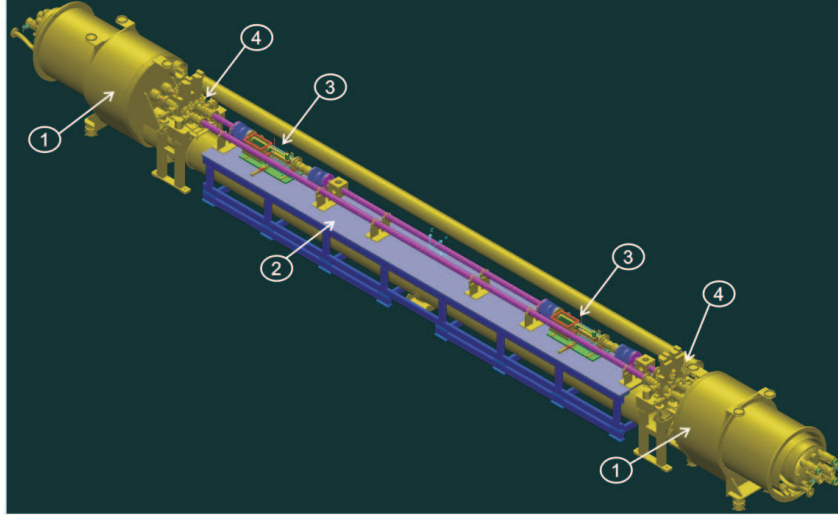
Figure 4.1: Schematic view of the connection cryostat (1) and detector arm with support table (2), two detector sections (3) and vacuum pumping sections (4).

and motor design can be adopted with little modification.

In this document, we will only present the main features of the movable beam pipes. More detailed information can be found in the FP420 design report [1].

4.2   FP420 moving pipe design

Figure 4.1 shows the layout of the connection cryostat at 420 m including two detector stations and the support table. The detector arm is fixed on the support table, which is attached to the tunnel floor, independent of the cryostat. Both ends of the detector arm are equipped with vacuum pumping and control stations and isolation valves. Figure 4.2 shows one of the two detector stations equipped with timing and silicon detectors, an LVDT (Linear Variable Differential Transformer) for position measurement and one moving and one fixed beam position monitor (BPM). The support table and motion system are shown in Fig. 4.3.

Each station is composed of a beam-pipe with inner diameter of 68.9 mm, wall thickness of 3.6 mm and two pockets of lengths 200mm for the
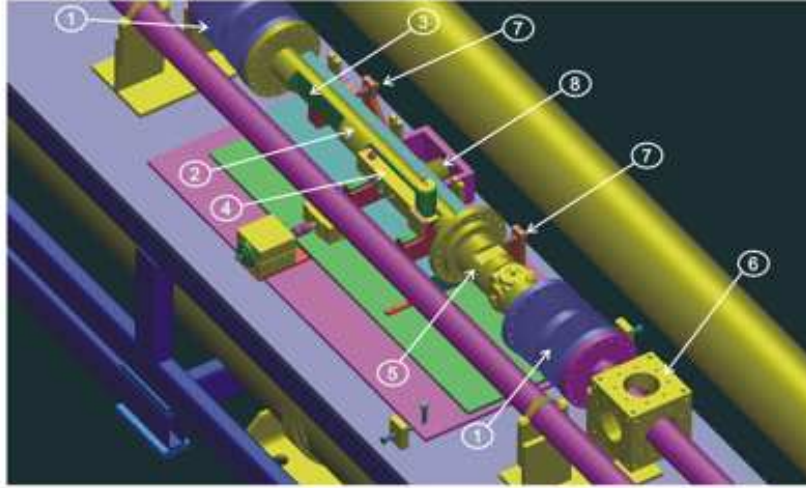
Figure 4.2: Top view of one detector section: bellows (1), moving pipe (2), Si-detector pocket (3), timing detector (4), moving BPM (5), fixed BPM (6), LVDT position measurement system (7), emergency spring system (8).

silicon detectors and 360 mm for the fast timing detectors, fixed on a motorised drive. Rectangular thin-walled pockets are built into the pipe to house the different detectors that must be positioned close to the beam. The displacement between data taking position and the retracted or parked position is 25 mm. The ends of the moving beam-pipes are connected to the fixed beam-pipes by a set of two bellows.

4.3   Pocket design and tests

A key factor in the pocket design is the desire to maximise detector acceptance, which is achieved by minimizing the distance of the detector edge from the LHC beam. This in turn requires that the thickness of the detector pocket wall should be minimised to limit the dead area. Care must be taken to avoid significant window deformation which could also limit the detector-beam distance.

A rectangular shaped detector pocket is the simplest to construct, and minimises the thin window material perpendicular to the beam which can cause multiple scattering and degrade angular resolution of the proton track.
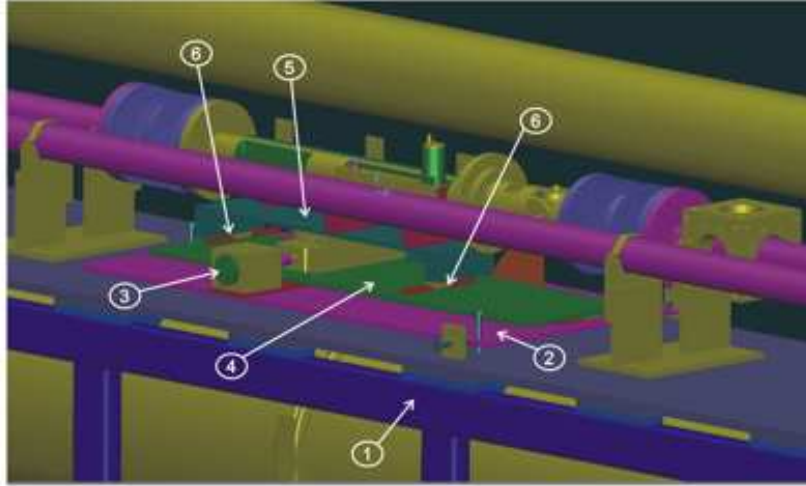
43

Figure 4.3: Support table (1), drive support table with alignment system (2), drive motor (3), intermediate table for emergency withdrawal (4), moving support table (5), and linear guides (6).

Only stainless steel beam tubes are suitable. They will be copper coated for RF-shielding and Non-Evaporative Getter (NEG) coated for vacuum pumping.

The deformation of a 600mm long pocket was measured by FP420 [1]. The magnitude of the deformation was less than 100 μm. The final design calls for pockets of 200 mm and 360 mm, implying significantly less deformation.

The baseline prototype of the moving beampipe was prepared for use in test beam at CERN in October 2007. Figure 4.4 shows the 1 m long beam-pipe equipped with two pockets, one of 200 mm length for the 3D pixel detector (Section 5) and the other of 360 mm length for the gas Čerenkov timing detector (Section 6) . The vacuum window thickness was 0.4 mm. A detector box for the 3D detectors was mounted in the first pocket. The moving pipe was fixed on a moving table, driven by a MAXON motor drive and guided by two high precision linear guides. The relative position of the moving pipe was measured with two SOLARTRON LVDT displacement transducers, which have 0.3 μm resolution and 0.2% linearity.
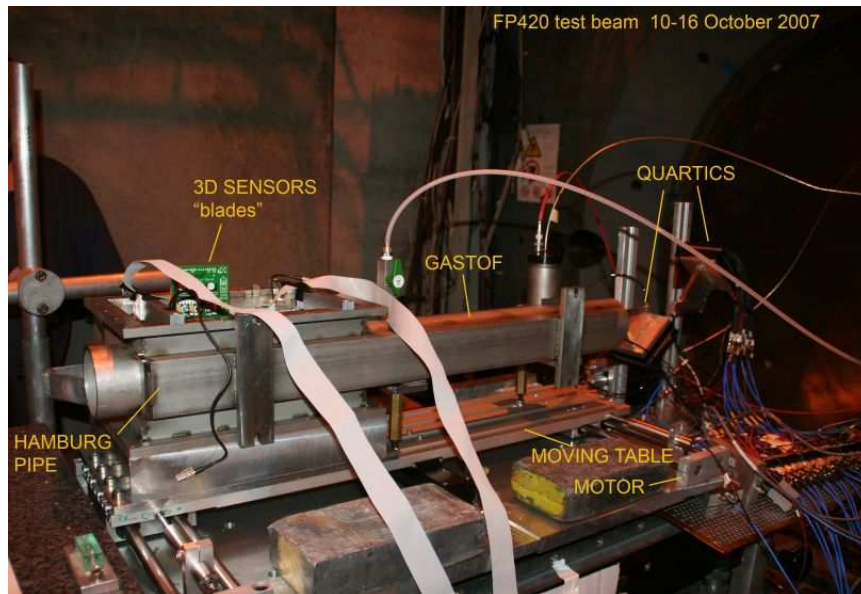
Figure 4.4: Photograph of the prototype beam-pipe section used in the October 2007 CERN test beam.

4.4 Machine induced backgrounds and RF effects

The safe distance of approach of the detectors to the beam depends on the beam conditions, machine-induced backgrounds, collimator positions and the RF impact of the detector on the LHC beams. So far, we have only performed detailed studies for the 420 m region; we do not anticipate significant RF impact, but the other issues warrant detailed study for the 220m case(in progress). The machine-induced background from near beam-gas and betatron cleaning collimation was found to be small, but at 420 m detector positions closer than 5 mm there is an appreciable background from far beam-gas, momentum cleaning collimation and proton loss in the beamline. Beyond 5 mm the integrated number of protons is expected to be less than one per bunch crossing, as shown in Fig. 4.5. The secondary neutron rate was found to be ∼ 0.1 per bunch crossing. More detail can be found in Ref. [1].

Extensive simulation and laboratory studies were carried out in Ref. [1] to test the impact of the 420 m detectors on the LHC impedance budget. The designs described above were found to have a negligible impact on the

LHC impedance budget, even at a distance of approach of 3 mm.

In summary, detectors at 420 m can operate safely and with low backgrounds at distances of approach beyond 5 mm. Similar studies are underway to determine safe operating parameters for the 220 m stations.
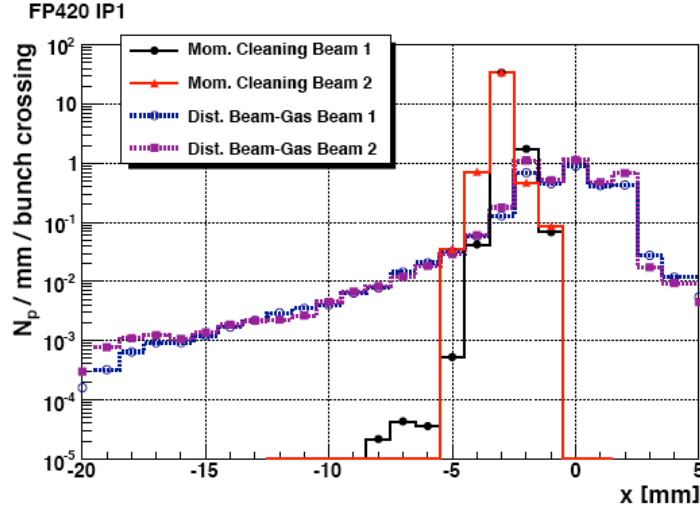
Figure 4.5: Number of protons per bunch crossing per mm at 420 m emerging from momentum cleaning collimators and beam gas interactions. (The protons here emerge in the $-x$ direction.)

4.5   Motorization and detector system positioning

In routine operation, detector stations will have two primary positions (1) the parked position during beam injection, acceleration and tuning, and (2) close to the beam for data taking. The positioning must be accurate and reproducible. Two options have been considered: equipping both ends of the detector section with motor drives which move synchronously but allowing for axial corrections with respect to the beam axis, or a single drive at the centre, complemented with a local manual axial alignment system. A two motor solution in principle allows perfect positioning of the detector station, both laterally and axially. However, it adds complexity to the control system, reduces reliability, and increases cost. Positioning accuracy and reproducibility are also reduced because extremely high precision guid-

ing systems can no longer be used, due to the necessary additional angular degree of freedom. Therefore, a single motor drive system has been chosen, accompanied by two precise LVDTs.

4.6   System operation and safeguards

The movable beam pipe detectors will operate at all times in the shadow of the LHC collimators in order to guarantee low background rates and to avoid detector damage from unwanted beam losses. Therefore, the high-level Hamburg pipe control system will be integrated in the collimator controls. The interface between low- and high-level controls will be implemented with the CERN standard Front End Standard Architecture (FESA) [68].

The LHC Control Room will position the detectors close to the beam after stable collisions are established. The precision movement system will be able to operate at moderate and very low speed for positioning the detectors near the beam. During insertion and while the detectors are in place, rates in the timing detectors will be monitored, as well as current in the silicon. The step motor and LVDT's will provide redundant read-back of the position of the detectors and fixed and moveable BPM's will provide information on the position of the detectors with respect to the beam. Separate mechanical alignment of the height and orientation with respect to the beam are discussed in Sec. 2.4.

4.6.1   Hamburg pipe summary and outlook

The Hamburg moving pipe concept provides the optimal solution for the 420 m and 220 m detector systems at the LHC. It ensures a simple and robust design and good access to the detectors. Moreover, it is compatible with the very limited space available at 420 m in the modified connection cryostat and with the expected position of the scattered protons between the two LHC beampipes. Its reliability is linked to the inherent absence of compensation forces and the direct control of the actual position of the moving detectors. Finally, rather large detectors, such as the timing devices, can naturally be incorporated into the pockets, which are simply rectangular indentations in the moving pipes. The prototype detector pockets show the desired flatness of the thin windows, and the first motorised moving section, with prototype detectors inserted, has been tested at the CERN test beam. This was a first step in the design of the full system, including assembling,

positioning and alignment aspects. A full prototype test is planned for Spring 2009 test beam.

It is important to note that the moving pipe design development and prototyping has been done in direct contact with the LHC cryostat group. In particular, the Technical Integration Meetings (TIM), held regularly at CERN and chaired by K. Potter, provided an efficient and crucial framework for discussions and information exchanges.

Chapter 5

Silicon Tracking Detectors

5.1 Introduction

In order to detect protons from the production of a central system of mass about 100 GeV, the detector edge at 420 m has to approach the beam axis to a distance of 5 mm (see Fig. 2.2). This represents a challenge for the radiation hardness and radio-frequency pick-up in the detector and the nearby front-end electronics. The detector system has to be robust, and for satisfactory control of systematic uncertainties its position has to be aligned and maintained to a positional accuracy of 10 μm in order to achieve the required track angular precision of 1μrad (see Section 2.3).

To maximise the acceptance for low momentum-loss protons, the detectors should be active as close to their physical edge as possible. In general, planar silicon detectors have a wide (0.25 mm – 1 mm) insensitive border region around the sensitive area that is occupied by a sequence of guard rings.

The key requirements for the tracking system at 220 and 420 m are the following:

- To track efficiently as close as possible to the sensor's physical edge.

- To have extreme radiation hardness. A design figure equivalent to or better than the vertex systems used for ATLAS will be required, i.e. better than 10^{15} 1-MeV equivalent neutrons per cm^2.

- To operate at the highest LHC luminosity and be robust and reliable.

- Individual detectors should have a spatial precision of ~ 10 μm. The tracking system angular precision should be 1 μrad.

- At 420 m the tracking detector needs to cover an area of 25 mm $\times$ 5 mm and at 220 m, the coverage should be of the order of 20 mm $\times$ 20 mm

3D silicon technology has been chosen as the baseline detector technology best equipped to meet the above requirements, although the tracking system has been designed such that any silicon technology compatible with the ATLAS pixel readout can be used. The backup technology is silicon strip detectors.

5.2   3D silicon detector development

3D Silicon detectors were pioneered by S. Parker (Univ of Hawaii, LBNL) more than 10 years ago [69]. Micro-machining techniques are used to produce narrow (5–25 μm diameter) holes orthogonal to the surface, typically spaced by 20–50 μm, filled with p or n-type conducting media, in order to produce a transverse electric field.

Using micro-machining techniques, electrodes penetrate the entire thickness of the detector perpendicular to the surface. This results in smaller collection distances, very fast signals, and substantially improved radiation tolerance. Figure 5.1 sketches the main features of the detector design. In addition, similar micro-machining techniques allow one to produce "active edges" where the amount of dead silicon at the edge of the detector is greatly reduced.

Full-3D silicon sensors have been successfully fabricated at CIS-STAN-FORD by J. Hasi (Manchester University) and C. Kenney (Molecular Biology Consortium) since 2001. The Manchester/MBC/Hawaii Collaboration has been working since 1999 to develop this technology for applications in particle physics. Important results are summarised below.

The first 3D detector used 16 rows of 38 p+ electrodes spaced by 100 μm with n+ electrodes locate 100 μm from the p+ electrodes. The total active area was 3.2 mm by 3.9 mm. The p+ electrodes were connected as strips to ATLAS SCTA readout chips. After tests in the X5 beam at the CERN SPS in 2003, the efficiency was found to be around 98% and particles were detected to within 5 μm of the physical edge. The full results of this beam test can be found in the TOTEM TDR [70] and Ref. [71]. A hybrid technology
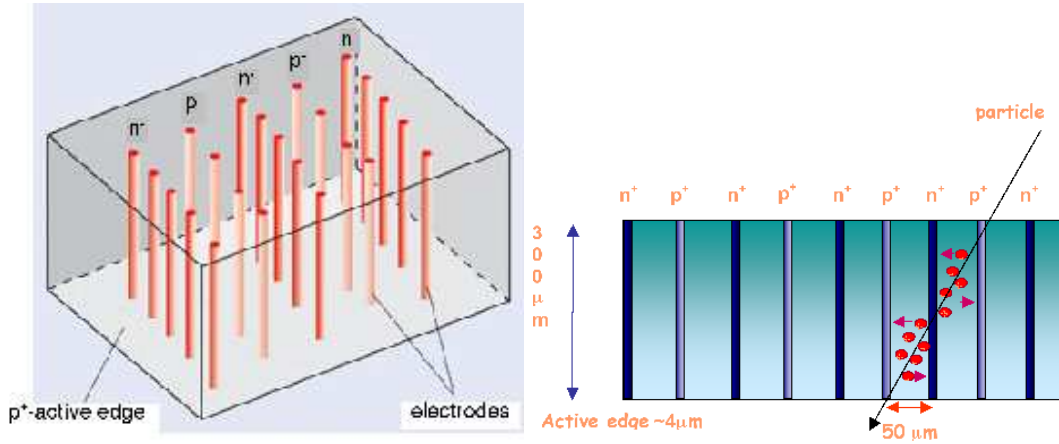
Figure 5.1: Isometric and lateral view sketches of a 3D detector where the p+ and n+ electrodes are processed inside the silicon bulk. The edges are trench electrodes (active edges) and surround the sides of the 3D device making the active volume sensitive to within a few microns of the physical edge.
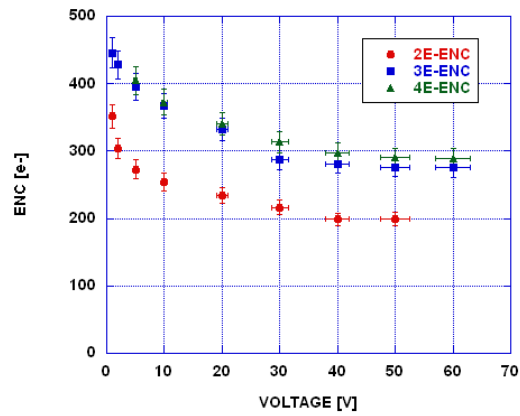

Figure 5.2: The equivalent noise charge (ENC) of the 2E, 3E and 4E 3D detectors after bump-bonding with the FE-I3 ATLAS pixel readout chip.
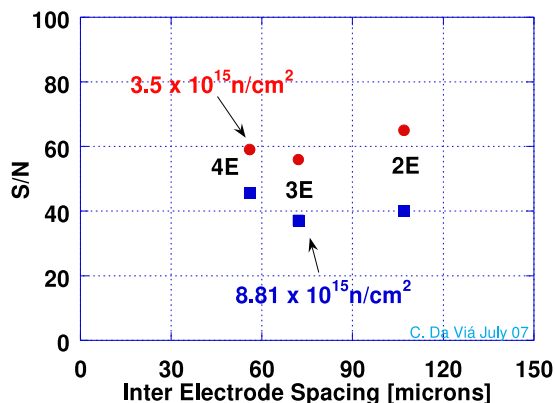
51

Figure 5.3: Extrapolated signal to noise (S/N) ratios of three 3D pixel configurations at two different irradiation fluences.

(planar/3D) detector was manufactured at Stanford and was successfully tested by TOTEM in a prototype Roman Pot at the CERN SPS in 2004. This uses planar technology but has a 3D active edge. This worked well, but is a factor 100 less tolerant to irradiation than full 3D technology.

Initial tests on irradiated 3D samples were made in 2001 [72]. The first results on the signal efficiency were obtained in 2006 using signal generated by an infrared laser. The 3D devices were irradiated with neutrons in Prague with an equivalent fluence of 10^{16} protons/cm^2 [73]. As expected, 3D devices can operate at much higher fluences than conventional silicon devices. For a minimum ionising particle, the signal size depends on the thickness. However, the signal collection distance is determined by the inter-electrode spacing, which can be as short as 50 μm. More information about these tests can be found in Ref. [1].

5.3 3D Silicon detectors at 220 and 420 m

The ATLAS Pixel Readout chip will be used both at 229 and 420 m. The 3D sensors with a total active area of 7.2 mm by 8 mm are bump-bonded to the readout chip. Operating voltages are a factor ten lower than for a standard

planar device and charge sharing only occurs very close to the pixel edge.

An extended collaboration (3DC) has been formed between Manchester, Hawaii, Oslo, SINTEF and the Technical University of Prague, to transfer this technology to industry and guarantee large scale production. Variations on the full 3D detector design are also being studied by IRST and CNM. Further developments are discussed in Ref. [74].

In order to understand the signal-to-noise performance for the various geometry detectors, the noise performance of the 3D sensors was measured after bump bonding with the FE-I3 ATLAS pixel readout chip. The equivalent noise charge (ENC) of the entire pixel matrix was measured, for each configuration, by injecting a variable amount of charge into each pixel front end and looking at the threshold dispersion over the entire matrix. This operation is possible since each front end electronics chip is equipped with a test input capacitance.

The extrapolated signal-to-noise of the three configurations after irradiation is shown in Fig. 5.3. The plot shows the S/N after a fluence of 3.5 $\times$ 10^{15} n cm^{-2} and 8.8 $\times$ 10^{15} n cm^{-2} respectively. The first set of values corresponds to the integrated fluence expected at 4 cm from the ATLAS interaction point (i.e. the ATLAS central tracker) after $\sim$10 years of operation of the LHC at nominal luminosity. The second set corresponds to the values expected after $\sim$5 years of operation at the same distance at the SLHC. These S/N results indicate that the lower fluences expected at the FP420 location should not compromise the performance of the 3D pixel tracking detectors. In conclusion, 3D detectors readout out using the ATLAS Pixel Chip fulfill all the requirements for use in the AFP experiment

5.4 Tracking detector mechanical support system

5.4.1 Layout at 420 m

The space available for the detectors is extremely limited. The baseline design is to have two independently moving pockets, one at each end of the 220 or 420 m regions. The pockets may be sub-divided to allow different cooling and vacuum conditions for the silicon and timing detectors. The design allows changes in the detector configuration to provide the optimal balance of detection points versus traversed material, and simple replacement of failing detectors during permitted tunnel access. To achieve an active area of 5 mm $\times$ 25 mm needed at 420 m requires a minimum of three silicon sensors. The basic detector unit, referred to as a superlayer, tiles the sensors to cover
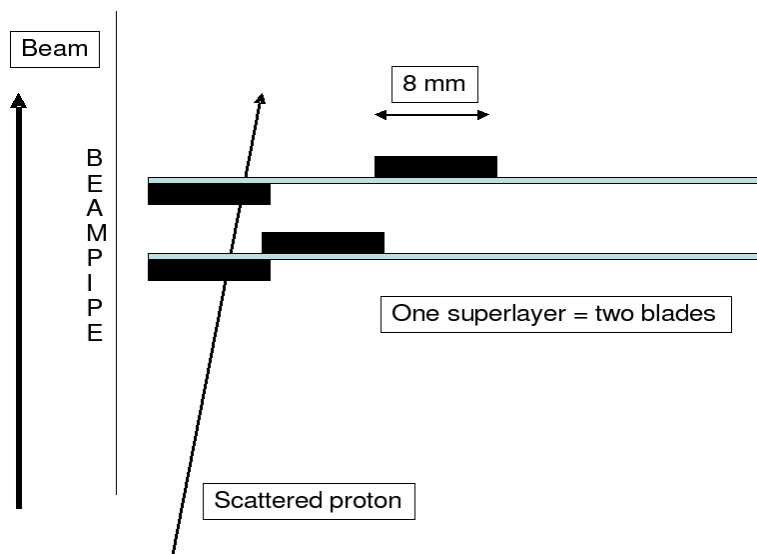
Figure 5.4: Schematic of a superlayer consisting of four sensors.

the required area. A superlayer is made of two "blades". Figure 5.4 shows a schematic of the superlayer layout to illustrate the basic geometry and nomenclature. A single tracking station will consist of a number of super-layers. Schematic drawings of a modular tracking station consisting of five superlayers are shown in Fig. 5.5.

Since the 3D silicon sensors have rectangular pixels of 50×400 μm, they have better position resolution along one axis. This means that superlayers can be designed to position the sensors to give superior resolution in the horizontal (x) or vertical (y) plane. The horizontal (x) deflection of the protons from the beam is of prime importance, since this corresponds to a measurement of the energy loss and hence the missing mass. The vertical (y) position becomes important primarily when the p_T of the outgoing protons is required.

To summarize, the detector at 420 m is made of 5 superlayers described in Fig. 5.7. Close to the beam, 10 layers of 3D silicon are available, whereas 8 mm further away, only 5 layers are considered. The best resolution is thus achieved close to the beam. Each superlayer can be staggered by 25 μm in horizontal direction. This leads to a space resolution of $50/2\sqrt{12} = 7$ μm in x-direction, and $400/\sqrt{12} = 120$ μm in y-direction close to the beam, and 240 μm further away.
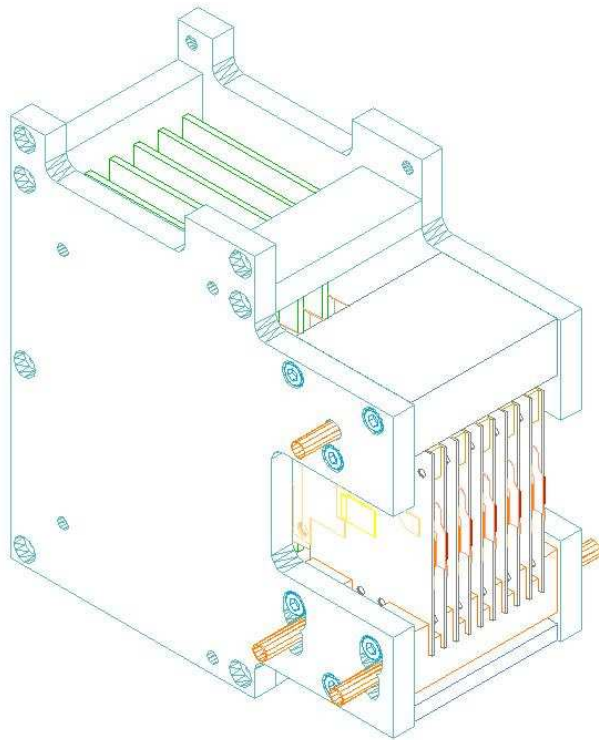
54

Figure 5.5: A five superlayer tracking station as implemented at 420 m. The mechanics supports the superlayers and also provides cooling blocks.

5.4.2 Superlayer and blade design at 420 m

A superlayer consists of two blades, each carrying two sensors. The two sensors closest to the beam overlap but are offset with respect to each other by half a pixel (25 micron) to improve track resolution for low ξ particles. A superlayer control card is positioned between the blades and connected by four flex circuits. Although the 3D silicon sensor technology is edgeless, tabs required for readout connections to the front-end ASIC, bias connections to the sensor and edge effects imply that it is impossible to tile the detectors in certain orientations. Even in the specific orientation unaffected by these tabs there are residual edge effects introduced by the front-end chip design. These constraints require detectors to be positioned over a number of overlapping layers to provide the required coverage. This is achieved by using both sides of the blade.

The choice of material for the blades is critical if the design goal of an internal mechanical alignment of 10 μm is to be achieved. The material must be stiff but machinable, have a high thermal conductivity and low coefficient of thermal expansion, similar to that of the attached silicon dies. The thermal conductivity must be optimised relative to the density to allow for extraction of heat from the detectors without too high a thermal gradient, whilst minimising the amount of material (radiation length) and hence multiple scattering.

Several blade design variants have been prototyped. The final design uses a CE7 frame and a decoupled planar thin front section supporting the detector. This allows the use of hard materials such as silicon or Al N whose thicknesses can be lapped down to 300 micron with high surface finish.

Thermal tests of the blades

Test blades have been built to investigate heat flow and thermal gradients and the resulting mechanical displacements using a thermal camera and a "smartscope" to measure the displacement. A realistic chip/glue/support interface structure was constructed using custom silicon resistors that match the size and power of the front end chip and have a similar bond pad layout. The preliminary thermal tests indicate that the blade design meets the required criteria of thermal and mechanical stability at the 10 micron level.

Assembly and alignment

The silicon sensors will be positioned on the blades using an adaptation of the automated assembly stages and jigs used to construct silicon modules for the ATLAS SCT at Manchester. The system uses automatic pattern recognition of fiducials on the readout chip to provide coordinates to x, y, θ motion stages which position the detector on precision jigs. Components are glued using a Sony CastPro dispensing robot under software control. The system allows silicon sensors to be reliably positioned on opposite sides of a blade with an absolute position accuracy of 5 μm. Detector blades are independently surveyed using a Smartscope optical coordinate measuring machine capable of one micron precision. Once the superplanes have been manufactured, the station needs to be assembled.

Linking individual blades together, in pairs as superlayers, and then into an entire station has some complexities. The reproducibility of repositioning a superplane is at the 5 μm level or better and is clearly demonstrated using the touch bearings.

To summarise: sensor to sensor positioning on a blade element can be achieved with an accuracy of 5 μm, and within a superplane to 10 μm.

5.4.3   Electrical details of the superplane

A flex circuit situated behind and bonded to the sensor is used to connect the FEC chips to the power supply and data lines via wire bonds. The flex circuit is fitted with a control chip (the MCC) which services the FEC chips, distributing clock, control and trigger information and collecting data for onward transmission. Aside from some slow single-ended signals, the connection between the FEC and MCC chips are implemented using LVDS-style differential signaling, with lower current than LVDS terminated into 600Ω. The two-layer flex circuit is built on a 50 μm polyimide core with a nominal track/spacing of 100 μm falling to 60 μm in the bond region, 100 μm laser drilled vias, and a Ni/Au finish suitable for Al wire bonding. The flex is pre-assembled (passive decoupling components soldered) then glued to the blade. Positioning is visual with respect to the chip and performed with a manual placement workstation with a typical accuracy of around 20 microns. The positioning is not critical, the bonding process can cope with many tens of microns misplacement between flex and the front end assembly. Aluminum (99% Al, 1% Si) wire with a 25 μm diameter is used.
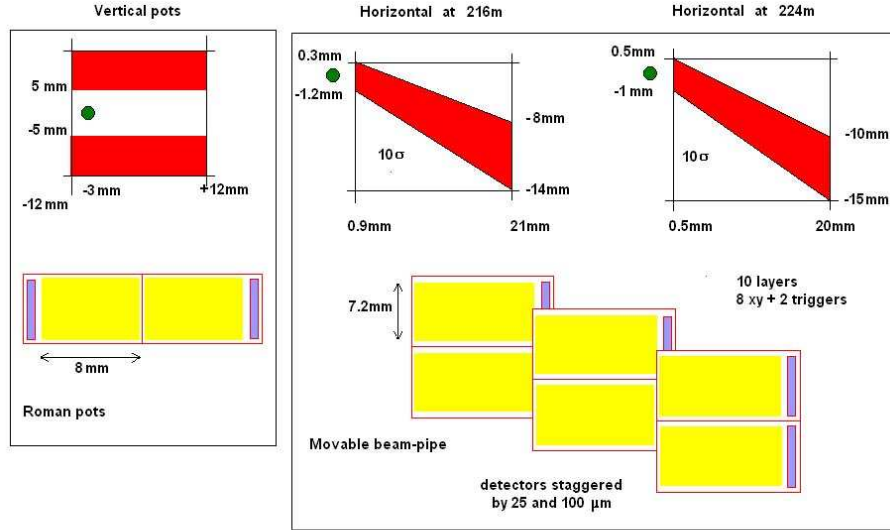
Figure 5.6: Acceptances and mapping of the silicon detectors. Each grey square corresponds to 10 staggered sensors for readout and 2 additional ones for trigger. We distinguish the horizontal detectors from the vertical ones (only needed if vertical roman pots are used for alignment purposes).

5.4.4   Silicon layout at 220 m

We propose to use the same sensors at 220 m. We will require a new blade and superlayer design, however, because the geometrical coverage and resolution requirements at 220 m are different than those required at 420 m. At 220 m the resolution must be better than 10 μm in x-direction and 20 μm in y. The main differences with 420 m detectors is shown in Fig. 5.6. At 220 m, larger silicon coverage is needed, with 60 sensors per detector optimised for the x measurements and 20 for the y measurement (to be compared with 20 in total at 420 m). The sensors are offset by 25 μm in x-direction and 40 μm in y. The resolution is $50/2\sqrt{12} = 7$ μm in x-direction, and $400/10\sqrt{12} = 12$ μm in y everywhere.

In addition, 12 additional sensors are needed for L1 trigger purposes for horizontal detectors and 4 for vertical ones. This would require modifications of the ATLAS pixel readout chip so that the information on the pixel line which has been hit can be transmitted to L1.

58
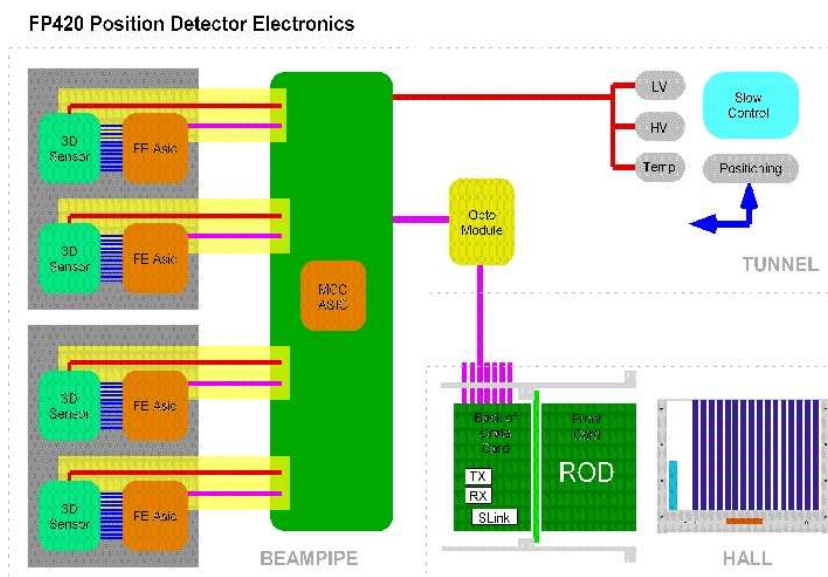
Figure 5.7: Layout of the readout and DAQ system.

5.5 Readout and infrastructure in ATLAS

5.5.1 ATLAS specific issues

Readout installations will be based on single-crate versions of the ATLAS silicon readout (see Fig. 5.7). Fibre connections from the tunnel arrive at optomodules fitted to a back of crate BOC card. The BOC provides timing adjustments and passes the data to the ROD where event segments are combined and DSPs can perform monitoring. Event data are passed back through the BOC to an SLINK transmitter and onward to the ATLAS standard ROS.

5.5.2 Tracker readout and downstream data acquisition

The 3D silicon assemblies and their readout take advantage of the significant design investment made by the ATLAS pixel groups. The bump-bonded detector assembly mimics an ATLAS pixel element and the downstream readout of the 220 and 420 m detectors can therefore be based very closely on the equivalent parts of the ATLAS pixel system. Each superlayer has independent connections to a support card situated within the support structure. LV

59

and HV are supplied from commercial units positioned nearby. Fibre optic data links to and from the central detector areas terminate on the support cards. Each station has its own link back to a ROD card that drives each arm of the 220 and 420 m detectors. The ROD crates are easily integrated into the ATLAS readout. An 18-bit pattern corresponding to the column having an hit (OR of 160 pixels) has to be sent at each beam-crossing (40 MHz).

5.6   Thermal design

Running detectors at -20°C implies that if they are not shielded from the tunnel environment they will ice-up. In order to prevent this from happening it is crucial to isolate these detectors from the LHC tunnel environment.

The enclosure can be kept under vacuum. Maintaining a vacuum around cold detectors is standard practice in laboratories, and the technology required to maintain this vacuum is bulk-standard, off the shelf. It will minimise the cooling requirements and it will minimise the thermal gradients.

The thermal requirements for the detectors are as follows;

- Lowest allowed operating temperature is -22°C.

- Nominal operating temperature is -20°C.

- Highest allowed operating temperature is -18°C.

- Required thermal stability during operation is better than 0.5^{o}C per 24 hours.

- The maximum allowed thermal gradient over an individual detector (chip) is 0.5^{o}C.

- All detectors within a test setup will be operating within 2°C of each other. That is, the temperature of the hottest detector at any given time is no more than 2°C higher than that of the coldest detector.

- The vacuum pipe, enclosing the LHC beam, will be at 30 degrees $\pm$ 5.

- The extreme temperatures to which the detectors will be exposed outside of operations will be the ambient temperature in the LHC tunnel and that during transport. These are expected to be in the range of 10 to 40°C.

The cooling system developed for the TOTEM project seems appropriate to cool the 220 and 420 m detectors as it has been designed and is acceptable for use in the LHC tunnel. It can reach the required cold-sink temperature with an adequate margin and has sufficient cooling power. The cooling system should be able to run for two years next to the LHC beam line, without servicing. The required cooling for operation in vacuum is specified as follows: 42 W pumping power at -90°C.

5.7 Performance of the tracking system

The performance of the tracker has been evaluated using a simple Monte Carlo program and also by a full GEANT4 simulation. In the GEANT4 simulation, the energy deposits within the sensitive detector volumes are translated into elementary charges and their collection on the electrodes is simulated. Capacitative coupling between closely placed channels as well as noise contribution are taken into account. The signal collected channel by channel is corrected by a gain factor, converted into an integer number and fed into a cluster-finding algorithm, if above a threshold. Clusters typically ($\sim$90% of the cases) include just one channel. The efficiency to find at least one cluster per plane is 99.7%. A resolution on the simulated hit position close to 10 μm has been measured for each plane. A track finding/fit algorithm based on a χ^2 fit loops over the available clusters.

Unlike central tracks, forward tracks have a very small angle. This means that hits in each tracking layer are highly correlated, consequently adding more layers does not improve the resolution by $1/\sqrt{N}$, where N is the number of layers. To improve the tracking precision, alternate layers will need to be offset by half a pixel width.

Figure 5.8 shows the angular resolution obtained from a simple Monte Carlo model. The multiple scattering angle is roughly 2 μrad $\times \sqrt{\text{thickness}/\text{X}_0}$) per layer at 7 TeV. If each layer corresponds to about 1% of a radiation length, then one has a multiple scattering contribution of 0.2 μrad per layer. For the materials in this model tracker, roughly 0.2% of the protons will interact per layer. Figure 5.8 shows calculations for a tracker consisting of N planes per station, with two stations placed 8 metres apart. The spatial precision per layer is 14 μm. Shifting alternate layers by 25 μm significantly improves the tracking performance. Using ten layers gives the design goal of one μrad, but more adding more planes actually degrades the resolution due to multiple scattering.
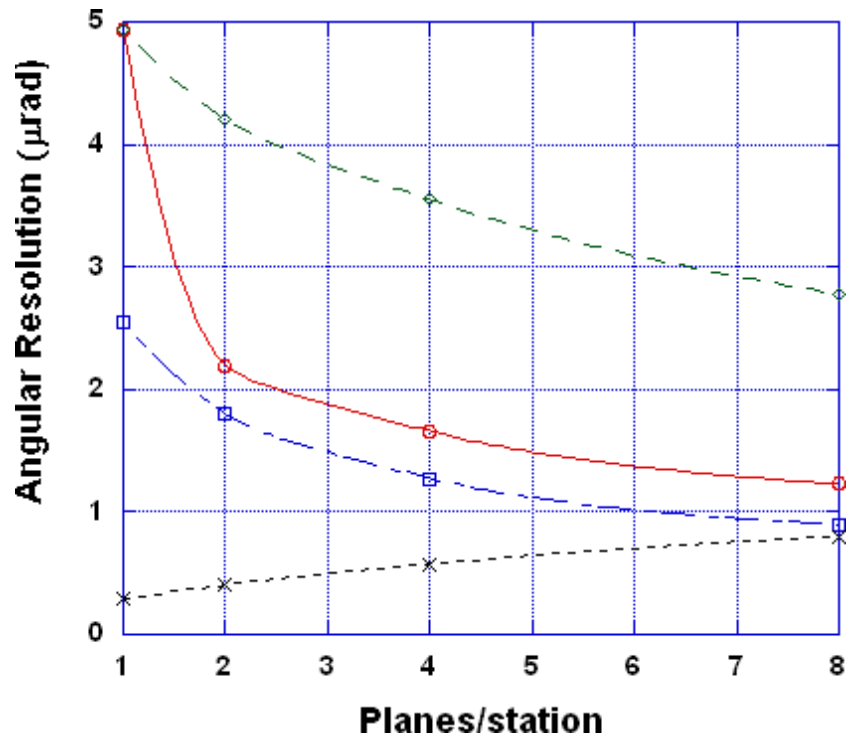
Figure 5.8: Angular resolution for a tracker consisting of two stations separated by 8 meters. Each layer has a detector with a pitch of 50 μm. The curves from top to bottom are: aligned tracking layers, alternate layers shifted by 25 μm, theoretical best result, and multiple scattering contribution. The design goal is 1.0 μrad.

The secondary interaction rate was evaluated as the fraction of proton tracks which have an inelastic interaction anywhere along the spectrometer before the last plane of the last station. It was found that in 1 mm of stainless steel, ceramic, and silicon the secondary interaction rates are 1%, 0.5% and 0.4%, respectively.

Figure 5.9 shows the χ^2/NDF and angular resolution for the two-station (0.85 μrad) and three-station (0.91 μrad) layouts. These are both within the design specifications. Finally, the efficiency of two-track reconstruction has been found to be 86% and 80% respectively for the two- and three-station layouts. Given that the three-station design provided more complexity without improving the performance, the two-station design was adopted.
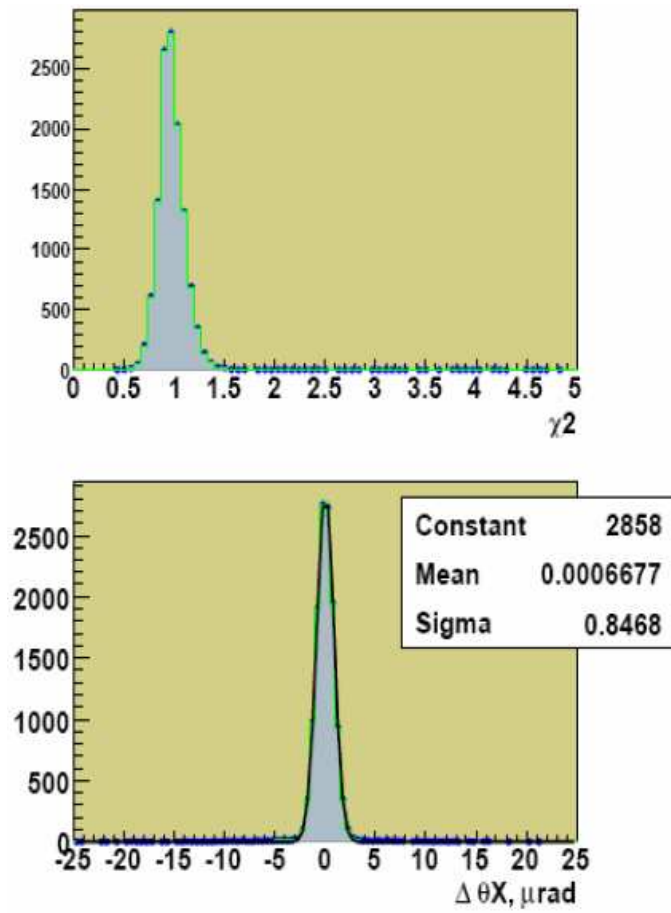
Figure 5.9: Track χ^2/NDF (top) and angular resolution (bottom) for a two-station tracker. The angular resolution is 0.85 μrad if the χ^2/NDF is selected to be less than 1.5.

Chapter 6

Fast Timing Detectors

The AFP detectors consist of timing detectors in addition to the silicon tracking detectors. In the initial phase of the project we plan to deploy timing detectors that can attain better than 20 ps resolution, which will be adequate for overlap background rejection (discussed below) in the initial period of data taking up to about 2012. The second phase of the project requires the best possible timing resolution, in the 5 to 10 ps range, to control the overlap backgrounds as the LHC approaches its design luminosity of 10^{34} cm^{-2}s^{-1}. Below we discuss the fast timing system planned for initial operations and the upgrade path for the second phase.

6.1 Overlap background and kinematic constraints

The AFP detectors must be capable of operating at the LHC design luminosity $\mathcal{L} \approx 10^{34}$ cm^{-2}s^{-1} in order to be sensitive to femtobarn-level cross sections in the central exclusive channel [pXp]. At these luminosities overlap background from two single diffractive events superimposed with a central hard scatter ([p][X][p]), as shown in Fig. 6.1(a) becomes a significant concern, especially in dijet final states. The 2-fold overlap coincidence backgrounds, shown in Fig. 6.1(b) and (c), also must be considered, however, as they scale with $\mathcal{L}^2$ instead of $\mathcal{L}^3$ they are less of a concern in the high luminosity limit. Fortunately, there are a number of techniques we can employ to reduce this overlap background. It can be substantially reduced at the high level trigger stage, or offline, by employing kinematic constraints. These factors include consistency between the central system and the protons in rapidity and mass, and also use the fact that the number of particle
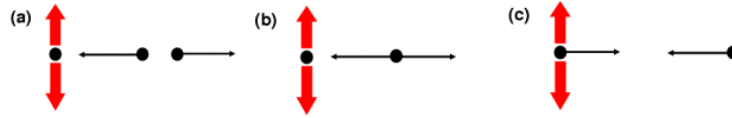
Figure 6.1: A schematic diagram of pile-up backgrounds to central exclusive production: (a) [p][X][p]: three interactions, one with a central system, and two with opposite direction single diffractive protons (b) [pp][X]: two interactions, one with a central system, and the second with two opposite direction protons (c) [p][pX]: two interactions, one with a central system and a proton, the second with a proton in the opposite direction.

tracks associated with the event vertex is much smaller for exclusive than generic collisions. Even after the significant background rejection afforded by these constraints, pile-up backgrounds are still expected to dominate the signals without the additional rejection provided by precision timing of the protons, as detailed below.

6.2   Timing

High precision time of flight (ToF) detectors can be used to obtain a large reduction in overlap (or pile-up) backgrounds [1]. It is necessary to measure only the *relative* arrival time of the two protons (denoted E for East and W for West, $\Delta t = t_E - t_W$. Under the assumption that they originate from the same interaction, the z-position of the event vertex can be calculated as $z_{pp} = \frac{1}{2}\Delta t \times c$. The uncertainty on the measurement of z_{pp} is $\delta z_{pp} = \frac{c}{\sqrt{2}}\delta t$, where δt is the (r.m.s.) time resolution of the proton measurement. For example, $\delta t = 10$ ps implies $\delta z_{pp} = 2.1$ mm. We then require a match between z_{pp} and the vertex position from the central detector, z_{vertex}, which is known with extremely good precision (≈ 50 μm) [85].

In the case of the overlap backgrounds, the protons do not originate from the same interaction as the hard scatter. Consequently, the vertex reconstructed from time-of-flight information will not typically be consistent with the vertex observed in the central detector. The resulting rejection factor depends on four parameters; the timing resolution δt, the spread in interaction points σ_z, the vertex window size, and the luminosity. The vertex window size is a trade-off between high signal efficiency (large window) and high background rejection (small window). Common choices are that the

vertices must coincide within 1, 1.5, or $2 \times \delta z_{pp}$, which corresponds to a signal efficiency of 68%, 87% and 95% respectively. The resulting rejection factor is larger for wider vertex distributions and is approximately linear with δt.

The prototype detectors described below have a timing resolution of $\delta t \leq 20$ ps. As the luminosity grows, better timing resolution is required. We envisage a program of detector upgrades to match this requirement, eventually attaining resolutions smaller than 10 ps, as discussed in Section 6.9. The relatively small and inexpensive precision ToF detectors discussed here make this approach viable.

We have calculated the background rejection for the three overlap cases shown in Fig. 6.1 (a) [p][p][X] (b) [pp][X] and (c) [pX][p]. For example, if $\delta t = 20$ ps ($\delta z_{pp} = 4.2$ mm) and the spread in interaction points is $\sigma_z \approx 50$ mm [85], we obtain a rejection factor of 21 for the first two cases and 15 for the third if the vertex measurement from proton time-of-flight is required to fall within ± 4.2 mm ($\pm 1 \times \delta z_{pp}$) of the vertex measured by the central detector. Case (a) dominates at high luminosity and consequently for $\delta t = 10$ ps, we would be able to obtain a rejection factor of greater than 40 (for a $\pm 1 \times \delta z_{pp}$ vertex window), enabling the detectors at 220 and 420 m to effectively cope with the large overlap backgrounds at the design luminosity. The final choice of vertex window will be optimised based on the analysis goals and instantaneous luminosity. For example, a discovery measurement would likely maximize signal to background, while the measurement of a state's properties, might demand very low background at the expense of signal efficiency.

In addition to detector performance, there are additional factors that could impact the overall timing precision. If the path length of protons detected in AFP were to vary significantly, this could degrade the vertex measurement accuracy. We have determined that even for the largest energy loss for protons in our acceptance, the path difference between different protons amounts to less than 30 μm, corresponding to a 100 fs time difference (even a smaller effect is expected from proton velocity differences). A second concern is that a precise measurement of the arrival time difference between deflected protons in the ToF detectors requires a reference timing signal at each detector with a $t_E - t_W$ jitter that is small enough not to contribute significantly to the overall time resolution. The large ToF detector separation of about 850 m makes this a challenging requirement. Our reference timing system, designed to yield an r.m.s. jitter of $\sigma_{LR} \approx 5$ ps, is described in Sec. 6.7.

6.3 Timing detectors

For quite a while the standard for time of flight detectors has been in the 100 ps range. Recently, there has been an explosion of interest in fast timing for medical purposes in addition to high energy physics detectors, and the idea of a detector with a few ps resolution is no longer considered unreasonable [86]. Indeed a time resolution of $\sigma = 6.2$ ps was recently achieved by a group from Nagoya [87] utilizing prompt Čerenkov radiation and micro-channel plate photomultiplier tubes (MCP-PMT). MCP-PMTs consist of a quartz faceplate and a photocathode followed by two back-to-back chevroned microchannel plates with small diameter holes (pores) that provide a uniform transit time for the photo-electrons. These devices can be read out by a single anode or multi-anode pads. They are compact (only about 3 cm in depth) and provide a typical gain of about 10^6. The Nagoya geometry does not suit our needs, but alternate detector concepts described below are likely capable of 10 ps or better resolution.

Three main factors affect the time resolution of Čerenkov detectors: (1) the spread in arrival time of photons at the photocathode, (2) the time resolution of the MCP-PMT, dominated by the transit time spread (TTS) of the electrons from emission at the photocathode to arrival at the anodes, and (3) the downstream electronics, including signal dispersion in cables. The first factor is minimised using Čerenkov light and optimised geometrical designs. The three major manufacturers of MCP-PMTs are Burle [88], Photek [89], and Hamamatsu [90] and all are capable of providing resolutions of less than 10 ps, given a sufficient number of photo-electrons.

We are developing two types of ToF counters for FP420, GASTOF (Gas Time Of Flight) and QUARTIC (QUARtz TIming Čerenkov). Prototypes of both types of detector have been built and tested.

A schematic diagram of the GASTOF detector developed at UC Louvain is shown in Fig. 6.2. It has a gas radiator at 1.3 bar in a rectangular box of 30 cm length, with a very thin wall adjacent to a specially designed flat pocket in the Hamburg beam pipe (Chapter 4). The protons are all essentially parallel to the axis. A thin 45° concave mirror at the back reflects the light to a MCP-PMT. The gas used in the tests, and which we propose to use in FP420, is C_4F_8O, which is non-toxic and non-flammable, and has a refractive index $n = 1.0014$ between 400 nm and 650 nm, giving a Čerenkov angle ($\beta = 1$) of 3.0°. C_4F_8O was first successfully used in a prototype RICH counter for BTeV [91].

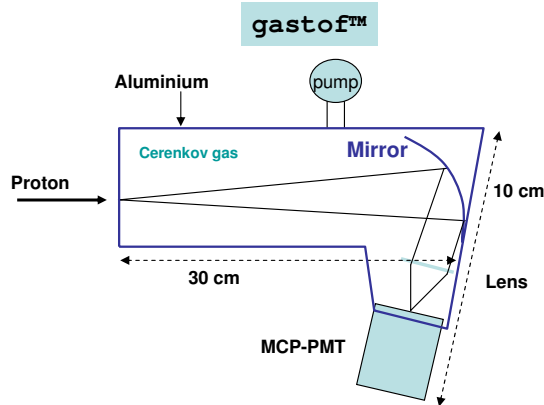The in-line material in a GASTOF (thin windows, mirror and gas) is

Figure 6.2: Schematic of GASTOF, a gas-based Čerenkov counter proposed by Louvain, as described in the text.

minimal and does not cause significant multiple scattering. It can therefore be placed between the tracking detectors without degrading the performance of the final tracking station. A key issue is the radiation hardness of the GASTOF detector, of which the main element of concern is the MCP-PMT. Lifetime tests on gain, transit time spread, and quantum efficiency under laser light irradiation were carried out at Hamamatsu and Budker Institute tubes by the Nagoya group [92]. At 2.8×10^{14} photons/cm^2 some gain decrease occurred (which would be recoverable by increasing the high voltage), but the TTS was not affected. A limitation of the current GASTOF design at high luminosities is that in the case of multiple protons it can only time the first one.

The QUARTIC detector, which utilises fused silica (artificial quartz) bars as radiators, is being developed by the University of Alberta, and the University of Texas, Arlington. Figure 6.3(a) shows the concept: a proton passing through the silica bars radiates photons which are measured by the MCP-PMT. Figure 6.3(b) shows the 4×8 array of bars with a 6 mm $\times$ 6 mm cross section and length ranging from about 100 mm for the first bar hit by the proton to 70 mm for the last. The bars are oriented at the average Čerenkov angle, $\theta_c \approx 48°$, which serves to minimise the number of reflections as the light propagates to the MCP-PMT. Figure 6.3(c) shows a third generation single-row prototype used in the June 2008 CERN test
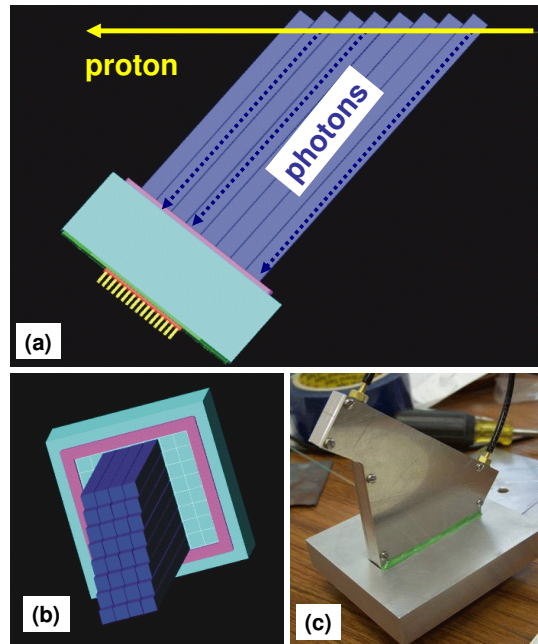
Figure 6.3: Conceptual drawings of a QUARTIC detector, (a) showing the proton passing through eight bars of one row in x providing eight measurements of the proton time (b) showing the 4×8 layout of QUARTIC bars (c) A photograph of the prototype detector used in the June 2008 CERN test beam.

beam. The final four-row version will have a very thin wall adjacent to the beam pipe, matching the dead area of the silicon detectors, to ensure full acceptance for all measured tracks. It will also use short tapered aluminised air light guides to channel the light into the respective pixels of the MCP-PMT. The x-segmentation of the QUARTIC detector will be useful to time multiple protons in the same bunch crossing, a consideration which becomes important at 220 m even for intermediate instantaneous luminosity.

Since the GASTOF and QUARTIC detectors have complementary features as discussed below, we are proposing to use both: one GASTOF detector will be located in its own beam pipe pocket after the first silicon detector pocket and two QUARTIC detectors will be located in their own pocket after the final silicon tracking detector, to mitigate the impact of multiple scattering.
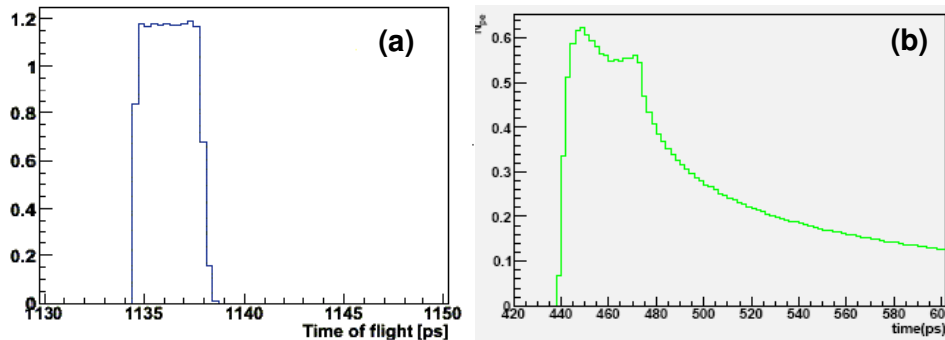
Figure 6.4: Simulated time of arrival of Čerenkov photons at the MCP-PMT photocathode for (a) GASTOF (b) QUARTIC.

6.4   Detector simulations

Figure 6.4(a) shows simulation results for the distribution of the arrival time of photons at the MCP-PMT face for a 30 cm long GASTOF. Due to GASTOF's optimised geometry and small Čerenkov angle all the photons arrive within a few picoseconds, consequently the time resolution is dominated by transit time jitter in the MCP-PMT and the subsequent electronics.

Figure 6.4(b) shows simulation results for the distribution of the arrival time of photons for a 90 mm long QUARTIC bar. For the QUARTIC bar the bulk of the photoelectrons arrive within 40 ps, and there is a long tail to much larger times. The width of the peak is due to the time dispersion from the wavelength dependence of the index of refraction in silica, while the long tail is due to photons emitted at different azimuthal angles, which leads to a variable path length. Both the GASTOF and the QUARTIC simulations show an expected yield after quantum efficiency of about 10 photoelectrons. Although the time spread for a QUARTIC bar is much larger than the GASTOF, the philosophy of the QUARTIC detector is to compensate for the inferior resolution of a single channel by performing multiple measurements. A proton traverses eight bars in each of the two QUARTIC detectors, giving 16 measurements with up to a 4-fold improvement in resolution over that of a single bar. A previous design with short silica bars and long air light guides to minimise time dispersion yielded a smaller number of photoelectrons due to reflection inefficiency and, in any case, is not suitable for AFP due to the larger active area needed at 220 m.

Ideas for combining the advantages of the two detectors to yield a seg-

mented detector with superior resolution for 2012 are being pursued and are discussed in Section 6.9.

6.5   Performance in test beam measurements

Test beam measurements over the last few years have validated the detector concepts (see Ref. [1]). Figure 6.5 shows the time difference between two GASTOF detectors (G1 and G2) from a 2007 test beam run, with $\delta t(G1 - G2) = 35 \pm 1$ ps (r.m.s.). If the two detectors were identical this would imply a 25 ps resolution for each. The G2 detector is superior to G1, however, due to an improved design resulting in a larger number of photoelectrons, and the use of a 6 μm pore Hamamatsu MCP-PMT which has a smaller transit time jitter than the 25 μm pore Burle tube. Analysis of the waveforms (recorded with a fast oscilloscope) gives a detector plus MCP-PMT resolution of $\delta t(G1)$ = 32 ps and $\delta t(G2)$ = 13 ps, close to the design goal. The recently completed 2008 test beam had silicon strip detectors that we used to study the efficiency as a function of position. Preliminary results give an efficiency of about 90% near the edge of the detector rising quickly to 99% at the center of the detector. The GASTOF readout electronics is discussed in the next section.

Figure 6.6 shows the time difference between two 90 mm long QUARTIC bars from the 2008 test beam run, with $\delta t(Q1 - Q2) = 56$ ps (r.m.s.). The signals from the MCP-PMT were passed through a custom-made constant fraction discriminator (CFD), and the resulting NIM pulses were recorded with a LeCroy 8620a oscilloscope. This result implies a QUARTIC bar resolution of 40 ps including the MCP-PMT and the CFD; taking the CFD resolution into account gives a 30 ps resolution for the bar/MCP-PMT combination. Preliminary studies show a uniform efficiency of near 90% across the bar. It is likely possible to increase the efficiency, by lowering the threshold of the constant fraction discriminator, and such studies are in progress using the raw waveforms. Given a 90% efficiency we would expect about 14 measurements per event for two 8-bar QUARTIC detectors, implying an overall resolution of about 11 ps for the QUARTIC detectors alone. This $\sqrt{N}$ dependence must still be demonstrated using a full detector row with the final detector and TDC system.
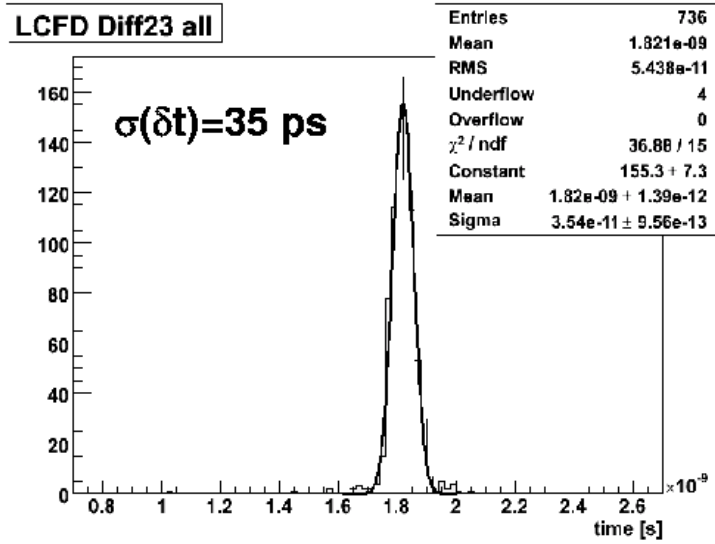
Figure 6.5: The time difference between the first (G1) and second generation (G2) GASTOF prototype detectors as described in text.
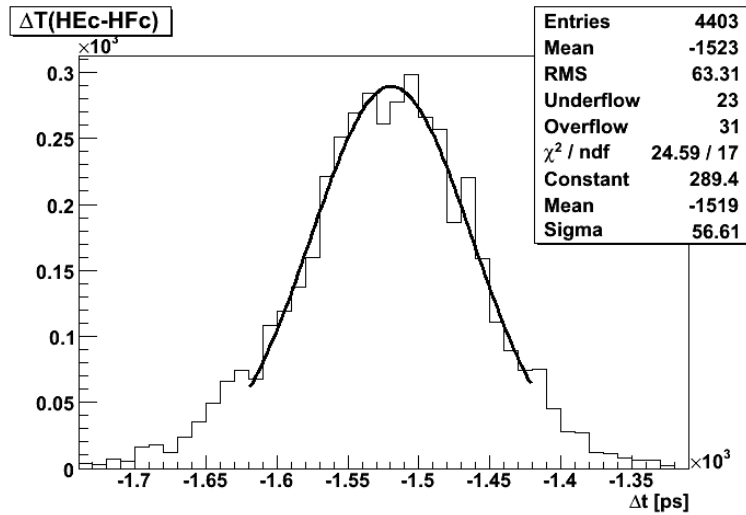

Figure 6.6: The time difference between two 90 mm long QUARTIC bars as described in text.

73

6.6 Electronics and data acquisition

The fast readout electronics must provide a timing resolution compatible with the baseline design of the ToF detectors. The Louvain group has developed the constant fraction discriminator that was used in the 2008 test beam. The Alberta group has developed a combined amplifer/discriminator board that has a performance comparable to commercial units, but is more compact and less expensive. Laser tests have yielded a preliminary resolution of 20 ps for the Alberta board, but this has not yet been tested in test beam, which has focused on oscilloscope-based readout. Alberta is also developing a custom readout system that employs the CERN-developed HPTDC chip that will interface with the ATLAS ROD readout system, and can employ either the Louvain or Alberta CFD. We plan to test a vertical slice of the AFP readout chain in spring 2009. We are also exploring other TDC options for when the TDC performance becomes a limiting factor. New ideas such as sampling the waveform to replace the discriminator/TDC functionality are also being pursued [86].

The single-channel GASTOF detector has an intrinsic detector/MCP-PMT resolution on the order of 10 ps, so requires a different electronics strategy to maintain this superior resolution. A single photon counter, such as Boston Electronics SPC-134, can be used to replace the amplifier, discriminator, and TDC, until the less expensive sampling chip is fully developed. Plans to adapt the Alberta interface board to include the GASTOF in the ROD readout have recently begun.

6.7 Reference time system

A reference time signal without significant jitter and skew between the East and West ToF detectors is an essential component of the ToF system. The goal of the design is to deliver a pair of synchronized trigger pulses to the detectors, which are physically separated by about 840 m, to a timing accuracy of 5 ps rms. This design uses long optical fibers to deliver pairs of low timing jitter trigger pulses to both ToF detectors. To minimize modal and group velocity dispersions, single-mode communication optical fibers and reliable industrial 10-Gbit Ethernet optical backbone components operating at the wavelength of 1.3 μm are used.

We rely on the high stability master bunch clock at CERN to derive our reference timing system. This master bunch clock is obtained from the

400 MHz superconducting RF cavity frequency, with a factor of ten divider synchronized to the revolution frequency. the delay between the edge of the master bunch clock and the passage of a bunch is fixed from run to run. This master bunch clock is a stable constant frequency square wave at 40.078879 MHz with a stability of 50 ppm corresponding to a 1.25 ps phase variation. Although this encoded bunch clock signal is broadcasted by the TTC transmitters around the CERN complex via single mode fibers (1.31 μm) to various LHC instrumentation and experiment areas, to minimize the added timing jitter and skew we design our reference time system starting at the stabilized reference electrical square pulse.

A block diagram depicting the various elements of this system is shown in Figure 6.7. A stable signal pulse is derived from the 40.078879 MHz bunch clock provided by the LHC Timing Trigger and Control (TTC) system. This RF signal is received by a programmable TTC receiver and to provide programmable post-skewing or de-skewing of the clock period in steps of 104 ps. Because the coincident RF trigger pulse arrives ~700 ns later than the proton-proton interaction, the post-skewing feature allows the triggers for the ToF detectors to be associated with the corresponding bunch crossings. It is desirable to select matched optical fiber components on both arms of the timing system to a path length accuracy of <1mm, corresponding to a 5 ps propagation delay, but any differences can be accounted for with calibration runs.

The time drift between both arms is expected to be dominated by environmental effects, primarily due to the 420 m length of the single-mode fibers. A variation of up 20 ps/ ^{o}C is anticipated for a 420 m single-mode fiber. Hence, all fibers and optoelectronics need to be housed in a temperature stabilized environment. The 40 MHz electrical pulse is converted to 1.3 μm optical pulse through a commercially available standard electrical to optical convertor. The optical pulse is then split to two replica in a non-polarization single-mode 2x2 splitter and sent along each of the ~420 meter long single-mode fibers to both East and West ToF detector stations. At each end of the optical fiber, the light pulse is further split to two, one to trigger the stop of the Time-to-Digital Converter (TDC), while the other is coupled to a Faraday mirror and retroreflected back to the source point through the 2x2 splitter. The returned pulse typically contains ~105 photons/pulse and is fiber-coupled to an optical correlator or an optical oscilloscope. At the input end of the optical correlator an amplified fast photodiode or a single-photon detector convert the optical pulses and displayed on an electronic sampling oscilloscope with a temporal resolution

of <5 ps. Alternatively, a >500 GHz optical sampling oscilloscope (Alnair Labs Eye-Checker) can be used which has temporal resolution of <2 ps and a timing jitter of < 0.1 ps. The time different between the rising edges of the two pulses δtref retroreflected from both arms is used as a feedback signal to drive a free-space delay scan stage deployed on one arm (West) of the $\sim$420 meter long optical path. The error signal from δtref is automatically adjusted to less than <5 ps rms (1.5 mm free space) for every bunch crossing. Prior to trigger the TDC, an Optical Constant Fraction Discriminator (OCFD), such as OFC-401, is used to suppress the electronic trigger delay shifts due to optical signal pulse amplitude variation. With this reference timing system, the two path of the trigger pulse for the ToF detectors can be synchronized to an absolute time difference of <5 ps rms. It is worth noting that this optical reference timing system is used to compensate mostly the slow environmental drift on the two arms of the trigger system.

So far we have designed a system which stabilizes spurious changes in the time difference measurement due to temperature and other sources of drift in the signal propagation to the 420 m detectors. For the comparison to central detector timing (see following section), we will also need to stabilize or measure the drifts in the average time of signal propagation to the two arms. We are currently evaluating options to do this. Perhaps the simplest way is to add an external trigger from the TTC/E-O converter to the optical correlator, then we can also record the time difference of either feedback signal relative to the trigger.

6.8 Central detector timing

To this point, we have been focussing on relative timing of the forward protons to provide a vertex position measurement for comparison with the position of the central vertex. It has been demonstrated in Ref. [93] that an absolute timing of the central detector portion of the event (two 60 GeV b-quark jets, for example) could provide a further overlap reduction factor for [p][X][p] events discussed earlier.

From a test beam analysis the ATLAS Electromagnetic Calorimeter (ECAL) was found to have a noise term of 500 ps/E(GeV) and a constant term of 70 ps. Reductions in the clock jitter could result in a smaller constant term during standard data taking. We have begun simulations to optimise and determine the ATLAS central detector time resolution. A 70 ps event resolution already would provide an additional factor of two in
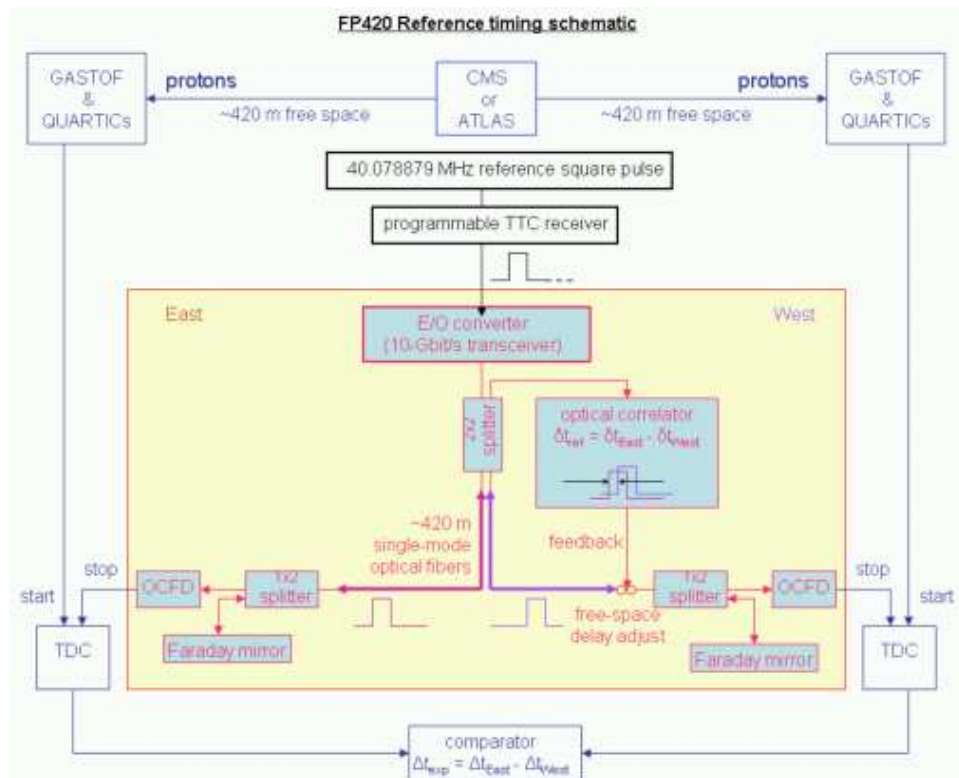
Figure 6.7: A schematic of the reference time system. Components labeled in black are expected to come from CERN TTC system, components labeled in blue are associated with the ToF detectors, and the components in red (highlighted in the yellow box) are the optical components related to the reference timing system.

overlap rejection, and if it is eventually possible to reduce this to 10 ps this factor grows to 12.

6.9 Timing summary and future plans

We are in the process of developing an ultra-fast TOF detector system that will have a key role in the AFP project by helping to reject overlap background that can fake our signal. Tests of the current prototype detector design imply an initial detector resolution of $\delta t \leq 20$ ps, including the full electronics chain, with an upgrade path to resolutions better than 10 ps matching the need for improved rejection as the luminosity increases. For a luminosity of $\mathcal{L} \approx 2\,10^{33}$ cm^{-2}s^{-1}, a 30 ps detector would be sufficient to keep the overlap background to the level of other backgrounds for the dijet channels, and render it negligible for other final states. For $\mathcal{L} \approx 5\,10^{33}$ cm^{-2}s^{-1}, a 10 ps detector (still with loose vertex cuts to maximise signal efficiency) would be desirable to keep overlap backgrounds totally under control, without any loss in signal efficiency. For $\mathcal{L} \approx 7\,10^{33}$ cm^{-2}s^{-1} to the design luminosity, we would control the background by (i) developing timing detectors in the 5 ps range, or (ii) adding extra rejection from central timing, or (iii) tightening the vertex window or other background cuts (a factor of several in rejection is possible with modest loss of efficiency), or more likely a combination of all of the above.

As the reference timing is also an important component of the timing resolution, we are also exploring other options for this, including interferometrically stabilised fibre optic links, where the standard is in the 10 femtosecond range.

6.9.1 Faster timing

The simplest approach to achieving faster timing is minor upgrades to the existing detectors. Further optimisation is possible through advances in MCP-PMT technology. The transit time spread of the MCP-PMT dominates the GASTOF resolution, so a pore size of 2 to 3 μm would already be expected to yield a time resolution below 10 ps. The addition of lenses to focus the light and a multi-anode design to allow timing of multiple protons are also being considered.

For the QUARTIC detector a next generation MCP-PMT with smaller pixel sizes would allow finer x segmentation for improved multi-proton timing. A smaller pore size would not be expected to dramatically improve the

time resolution, since the largest component is the intrinsic detector resolution, but might yield modest improvements on the 10-20% level. Better electronics (discussed below) could also give an incremental improvement, with the combination resulting in a sub 10 ps detector.

Hybrid detectors which combine the advantages of GASTOF and QUARTIC are also being considered. Saclay is investigating a design that would give a precise knowledge of the Cerenkov photon origin, and therefore a better timing accuracy. This design, in the early simulation phase, is comprised of a blade of MgF2 (refractive index 1.39), a focusing mirror, and a segmented MCP-PMT. The detector resolution might be limited only by the blade thickness (a 1 mm implies an uncertainty less than 3 ps) and could provide multi-proton timing using different pixels.

Improving the readout electronics should also yield improved timing performance. The University of Chicago (Henri Frisch, Fukun Tang and Jean-Francois Genat) are engineering transmission line readout coupling the anodes of the MCP-PMT to a printed circuit board where fast pulse sampling integrated devices will acquire digital pulse waveforms from which the mean time and the position could be obtained using digital signal processing [94].

Simulations comparing the time resolution obtained from various methods have been performed using synthesized signals from Micro-Channel Plates detectors. Figure 6.8 shows the timing resolution as a function of the sampling rate, for 30 and 100 input photo-electrons. The pulse sampling method is clearly superior to other techniques particularly for smaller number of photoelectrons, the regime of our detectors.

Sampling devices in the 1–10 GHz range have been pioneered by D. Breton at Orsay (France) for ATLAS, and developed by E.Delagnes at Saclay (France) [95], S. Ritt at PSI [96], and Hawaii by G. Varner [97]. A sampling chip is under development at the University of Chicago with support from Saclay, Hawai, and Orsay, and is expected to be available on the timescale of the next generation timing detectors.
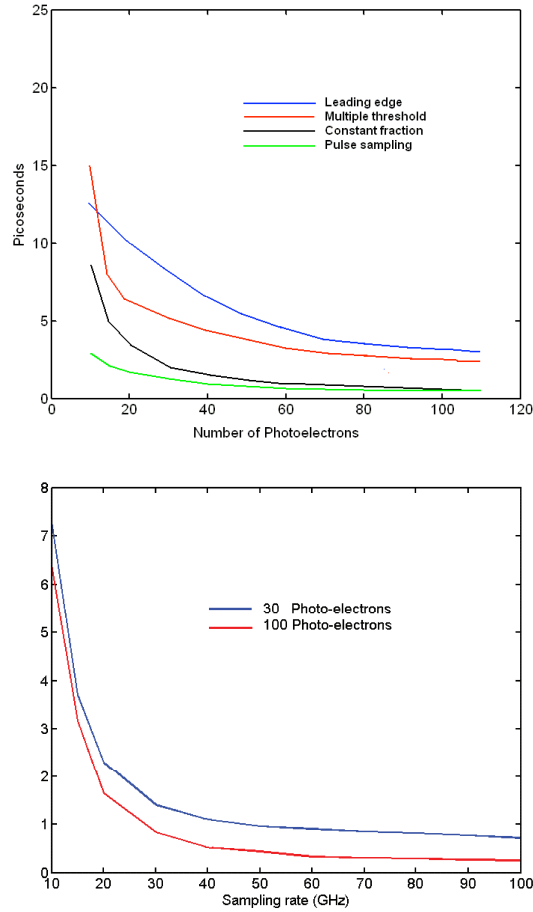
Figure 6.8: Top: Simulation of the timing resolution as a function of the number of photo electrons, using several timing techniques: leading edge, multiple-threshold, constant fraction, pulse sampling at 40 GHz. The pulse sampling performs best, and also provides the integral pulse charge, pulse shape, and the baseline for pileup. Bottom: Simulated time resolution as a function of the sampling rate for 30 and 100 input photo-electrons.

Chapter 7

Triggering with Forward Detectors at 220 m

It is possible to integrate the 220 m detectors into the ATLAS L1 trigger system. This allows for an enhanced trigger efficiency above that achievable using only the central detector and forward detector information at L2, as described in Section 1.1. For events with central masses above ~ 140 GeV, events may have at least one track in the 220 m system, depending on the distance of approach of the detectors to the beams (see Fig. 2.3). For masses above ~ 200 GeV, events may have a proton track in both 220 m detectors. The event topologies are shown schematically in figure 7.1. We emphasize that it is possible to trigger on the central detector alone for the majority of physics signatures of interest to ATLAS FP, using forward detector information from 420 m and 220 m detectors to reduce the rates at L2 where necessary. It is however desirable to increase the trigger efficiency where possible, particularly at high luminosity and particularly for purely hadronically decaying final states such as high-mass $H/h \to b\bar{b}$ in the MSSM (see Fig. 1.3). In this chapter we outline the expected trigger rates and a conceptual design of the trigger system.

7.1 Trigger implementation

The 220 m detectors can provide a trigger signal to ATLAS L1. In each station, two planes of 3D silicon pixels will be read out in a strip mode oriented in the vertical direction via a fast dedicated electronics read out (FAST OR) devoted exclusively to the trigger. The AFP L1 trigger is per-
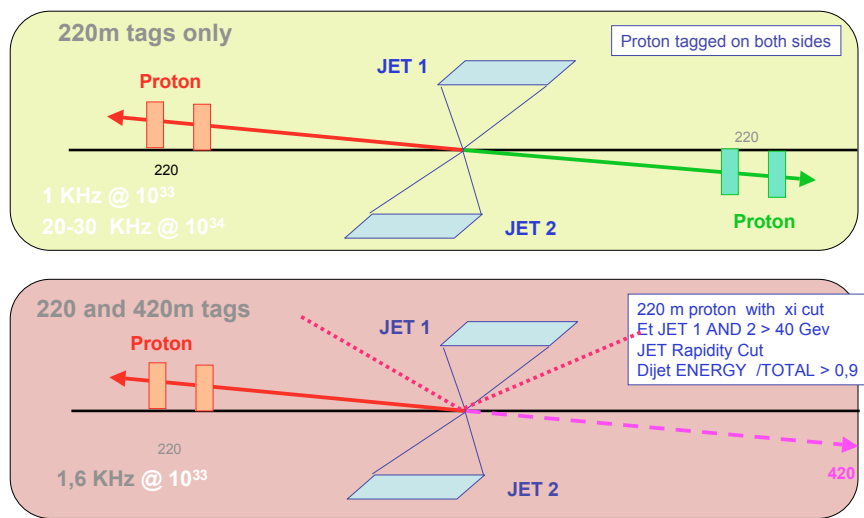
Figure 7.1: Illustration of the L1 trigger topology for the cases in which both protons are tagged at 220 m (top) and when only one proton is tagged (bottom).

formed in two steps. First, in each station, a local coincidence between the two silicon trigger planes is requested. Second, a hodoscope-like track segment is constructed from the trigger hits at each end of the Hamburg Pipe to check if the hits are compatible between the four trigger layers to allow real events to be distinguished from noise. The L1 input coming from the AFP detector is thus the address of the pixel hit in the x-direction, which is directly proportional to the ξ of the proton. We distinguish two possible L1 triggers from AFP:

- a single diffractive trigger where only one proton on one side is requested. This trigger is interesting for "hybrid" events where one proton is tagged at 220 m and the other one at 420 m. We cut on the pixel x-position for those events, which corresponds directly to a cut on ξ.

- a double pomeron exchange trigger where both protons are requested to be tagged at 220 m. For these events, we will cut on the x-position of the pixels on each side, or in other words, on the ξ of both protons which is directly related to the mass of the centrally produced object.

The AFP L1 elements on each side of ATLAS will be sent to ATLAS through a fast direct high speed cable or fiber to minimize the time of flight, and both elements will be combined for the L1 AFP trigger. The AFP trigger signal has to be integrated into the present ATLAS trigger scheme (75 kHz maximum rate, 2.5 microseconds latency) as shown in Fig. 7.2. The decision must be made within 100 ns, which leaves enough time taking into account the particle's flight path and transit cables from the tracking stations.

When a positive trigger decision from ATLAS is reached (even if no diffractive trigger has been issued), the 3D detectors will be read out and the data assembled in a Read out Driver (ROD). This requires that the buffer of the read out chip has to be large enough to accommodate an extended time delay associated with the time to reach both 220 m and 420 m, in addition to the L1 trigger latency. The implementation block diagram is shown in Fig. 7.3.

7.2 AFP Trigger strategy and rates

7.2.1 Trigger strategy

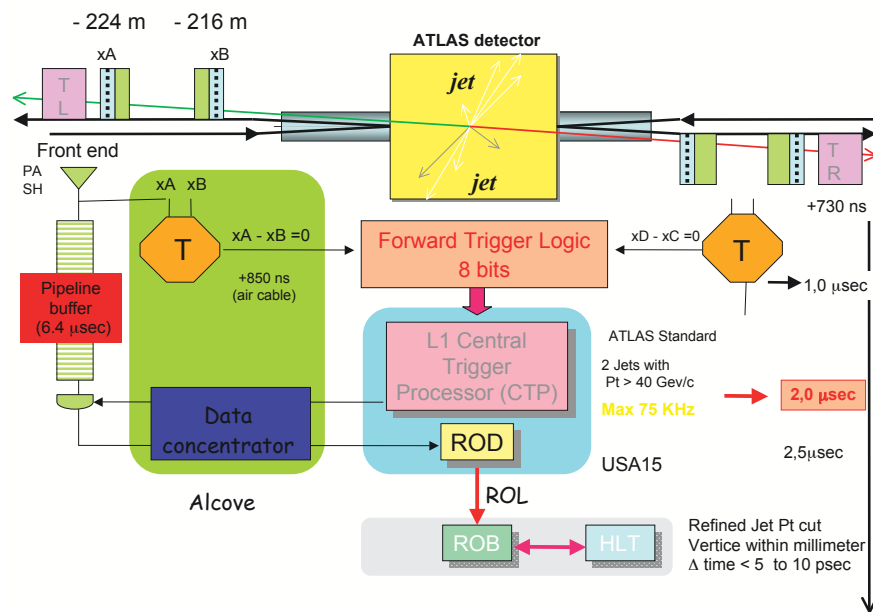An example trigger strategy at the first level (L1) using the forward detectors at 220 m is the following:

Figure 7.2: Diffractive trigger topology. The trigger defined at each station on each side of ATLAS is sent to the ATLAS L1 trigger.
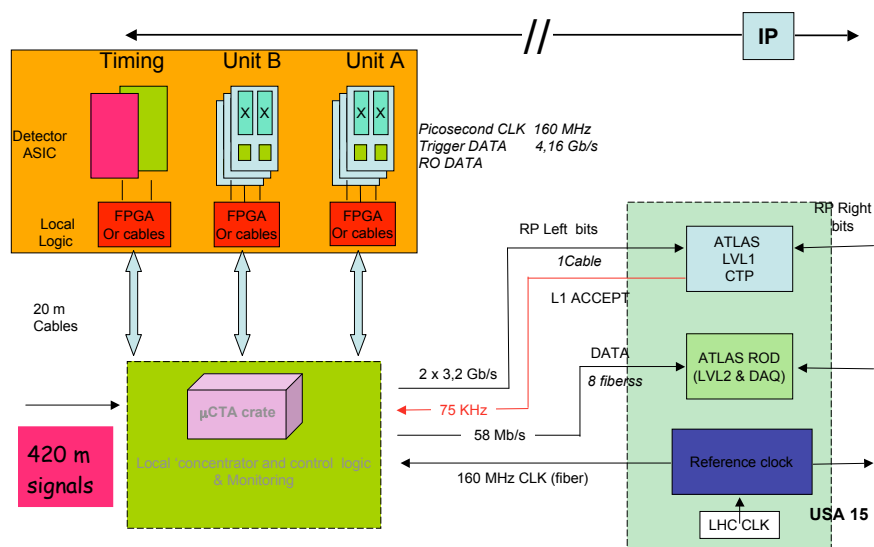
Figure 7.3: Trigger and readout implementation in ATLAS

- Inclusive double track trigger: it will be possible to trigger inclusively on events with tracks in both 220 m detectors even at the highest luminosity for high central masses ($M > 1$ TeV). This trigger does not request any special high p_T activity (lepton, jets...) in the central ATLAS detector. This will be the only inclusive trigger in the experiment.

- Double pomeron exchange trigger with high p_T activity in the ATLAS detector. This trigger requires two diffracted protons ($\xi > 0.02$ to be in the acceptance of the 220 m detectors), and two high p_T jets ($p_T > 40$ GeV), or at least one high p_T lepton ($p_T > 5$ GeV) in the central ATLAS detector. This trigger could be used for central systems of all masses within the acceptance of the 220 m detectors.

- Single track in one 220 m detector. This trigger corresponds to double pomeron exchange events where the second proton is tagged at 420 m. This has the highest rate and will be studied in more detail in Section 7.2.2. This trigger could run unprescaled up to 2.10^{33}.

- Single track trigger to perform QCD and photo-production studies: this trigger will request only one proton tagged at 220 m and will generally be prescaled.

As discussed in Section 1.1, information from the 420 m detectors can be used at L2 to reduce the trigger rates to a few Hz even for the most challenging dijet final state scenarios.

At high luminosity the trigger rate is dominated by pile up events when a proton is produced in a secondary single diffractive interaction. There will be a proton track in one 220 m detector in 2.3% of events at an instantaneous luminosity of 2×10^{33}cm^{-2}s^{-1}. The probability to tag a proton on each side of ATLAS in 220 m detectors at 10^{34}cm^{-2}s^{-1} is over 30%, which means that an inclusive L1 double track trigger at the highest luminosity using forward detectors will not be possible.

7.2.2 Triggering on low mass central systems using one 220 m track at L1

The most difficult scenario for the AFP, but potentially a very interesting one, is Higgs production and decay to two b-quarks. As discussed in section 1.1, the observation of the Higgs boson is possible in this channel across a

wide range of MSSM parameter space using a trigger based entirely on the ATLAS central detector, with a veto at L2 based on tracking information from the 220 m and 420 m detectors. For masses in excess of ~ 140 GeV, however, information from the 220 m detectors will be available at L1, and this could be used to increase the trigger efficiency. It is clear from Fig. 1.3 that such a strategy would be valuable across a large area of the m_a - $\tan\beta$ plane. A proposal for the L1 trigger in this scenario is the following:

- require one jet with $E_T > 40\,\text{GeV}$ (expected rate is $2.6\,\text{kHz}$ at $\mathcal{L} = 10^{32}\text{cm}^{-2}\text{s}^{-1}$, or $260\,\text{kHz}$ at $\mathcal{L} = 10^{34}\text{cm}^{-2}\text{s}^{-1}$)

- Requirement of exclusiveness: $(E_{T1} + E_{T2})/H_T > 0.9$, where H_T is the scalar sum of all L1 jet transverse momenta (a reduction factor of about 2, which is almost independent on luminosity)

- Require a proton in one of the two forward spectrometers at $220\,\text{m}$

- Require that $(\eta_1 + \eta_2) \cdot \eta_{220} > 0$, where $\eta_{1,2}$ are the pseudorapidities of the two L1 jets, and η_{220} is the pseudorapidity of the proton that hit the 220m forward detector (this requirement ensures that the second proton is within the acceptance of the 420 m detectors, which is the only case of interest for a Higgs search).

- Require the fractional momentum loss of the proton in the 220m detector to be $\xi < 0.05$ (due to the 420m detector acceptance in ξ, the proton momentum fractional loss in the 220m detector cannot be too high).

Let us note that some part of this trigger would need an upgrade of the ATLAS trigger which does not allow at present to access the jet rapidity. Not applying this cut would increase the rates by a factor 2, and the signal will have to be prescaled accordingly. If all cuts can be performed, such a trigger can be run at a L1 rate of about $1\,\text{kHz}$ for luminosities up to $2 \times 10^{33}\,\text{cm}^{-2} \cdot \text{s}^{-1}$ which corresponds to 7 proton-proton interaction per bunch crossing. The estimated rejection factors are given in Tab. 7.1. For higher luminosities, the trigger would be pre-scaled appropriately, and the availability of the 420 m information at L2 would allow for a reduction of the rate to below a few Hz, as for the 420 m + 420 m case discussed in section 1.1.

87

$\mathcal{L}$ $E_T > 40\,\mathrm{GeV}$	n_{pp} per bunch crossing	1 jet rate [kHz] $[\mathrm{cm}^{-2}\cdot\mathrm{s}^{-1}]$	RP200 reduction factor	$\xi < 0.05$ reduction factor	Jet Prop.
1×10^{32}	0.35	2.6	120	300	1200
1×10^{33}	3.5	26	8.9	22	88
2×10^{33}	7	52	4.2	9.8	39.2
5×10^{33}	17.5	130	1.9	3.9	15.6
1×10^{34}	35	260	1.3	2.2	8.8

Table 7.1: L1 rates for 2-jet trigger with $E_T > 40\,\mathrm{GeV}$ and additional reduction factors due to the requirement of triggering on diffractive proton in 220 m detector, and also on jet properties.

7.3   Summary

It is possible and desirable to implement a L1 trigger for the 220 m detectors. Such a trigger would enhance the discovery potential of ATLAS FP, in particular for Higgs bosons decaying to b-quarks for a wide range of MSSM scenarios.

Chapter 8

Conclusion

8.1   Cost estimate

A preliminary estimate of the costing of the major components of the 420 m detectors is given here as an indication. A detailed costing evaluation is still being performed.

- Two new cryostats per experiment, amounting to a total of 1.5 MCHF

- The silicon tracker including the electronics and mechanical parts: 0.7 to 1.0 MCHF, depending on the purchasing of equipment

- Quartic timing detectors, including electronics, 100 kCHF for 4 detectors.

- GASTOF timing detectors, including electronics, DAQ, slow controls and cables: 145 kCHF

- BPMs and beampipe mechanics: 380 kCHF

- High voltage/Low Voltage: 160 kCHF

This leads to a approximate grand total of 5 MCHF for equipping both sides with 420 m and 220 m detectors.

8.2   Summary

We propose to install four forward proton detector stations around ATLAS; one on each side of the IP at 220 m and 420 m. Such detectors would allow

for an extension of the baseline ATLAS physics program, including a possible direct measurement of the quantum numbers of SM and MSSM Higgs bosons and high precision mass measurements of new particles including Higgs bosons and supersymmetric particles. For particles with masses below ~ 160 GeV, the resolution will be ~ 2.5 GeV *per event*, irrespective of the decay channel of the central system. For higher mass states in which one proton is detected at 220 m and the other at 420 m, the resolution will be ~ 5 GeV per event. In certain regions of the MSSM and NMSSM, forward proton tagging could be the Higgs boson discovery channel. In addition, a rich TeV-scale electroweak and QCD physics program would be possible.

We propose to use the detector design developed by the joint ATLAS/CMS FP420 R&D Collaboration at both 420 m and 220 m. At 420 m, the installation requires a cryogenic bypass which has been designed by the CERN TS/MME group. The design integrates a high-precision silicon tracking system and fast timing system capable of detecting the arrival time of protons with an ultimate goal of better than 10 ps precision. Such a system would be able to operate at instantaneous luminosities up to 10^{34}cm^{-2}s^{-1}.

The detectors at 220 m would be integrated into the ATLAS L1 trigger system. Both the 220 m and 420 m detectors would be integrated into the HLT, providing significant rejection at L2.

Upon approval of the LOI, we would plan to proceed towards a TDR aiming to attract sufficient collaborators and funding to build the full system in time for a potential installation during the winter 2010 shutdown.

Bibliography

[1] M. G. Albrow *et al.* [FP420 R&D Collaboration], arXiv:0806.0302 [hep-ex].

[2] A. Bialas and P. V. Landshoff, Phys. Lett. B **256** (1991) 540.

[3] J. R. Cudell and O. F. Hernandez, Nucl. Phys. B **471** (1996) 471 [arXiv:hep-ph/9511252].

[4] V. A. Khoze, A. D. Martin and M. G. Ryskin, Eur. Phys. J. C **23** (2002) 311 [arXiv:hep-ph/0111078].

[5] B. Cox, J. R. Forshaw and B. Heinemann, Phys. Lett. B **540** (2002) 263 [arXiv:hep-ph/0110173].

[6] A. De Roeck, V. A. Khoze, A. D. Martin, R. Orava and M. G. Ryskin, Eur. Phys. J. C **25** (2002) 391 [arXiv:hep-ph/0207042].

[7] A. B. Kaidalov, V. A. Khoze, A. D. Martin and M. G. Ryskin, Eur. Phys. J. C **33**, 261 (2004) [arXiv:hep-ph/0311023].

[8] B. E. Cox, J. R. Forshaw, J. S. Lee, J. Monk and A. Pilaftsis, Phys. Rev. D **68** (2003) 075004 [arXiv:hep-ph/0303206].

[9] J. R. Forshaw, arXiv:hep-ph/0508274.

[10] M. Boonekamp, C. Royon and R. Peschanski, Nucl. Phys. A **755**, 599 (2005).

[11] J. R. Ellis, J. S. Lee and A. Pilaftsis, Phys. Rev. D **71** (2005) 075007 [arXiv:hep-ph/0502251].

[12] P. J. Bussey, T. D. Coughlin, J. R. Forshaw and A. D. Pilkington, JHEP **0611**, 027 (2006) [arXiv:hep-ph/0607264].

[13] V. A. Khoze, A. D. Martin and M. G. Ryskin, arXiv:0705.2314 [hep-ph].

[14] V. A. Khoze, A. D. Martin and M. G. Ryskin, Phys. Lett. B **650**, 41 (2007) [arXiv:hep-ph/0702213].

[15] S. Heinemeyer, V. A. Khoze, M. G. Ryskin, W. J. Stirling, M. Tasevsky and G. Weiglein, Eur. Phys. J. C **53** (2008) 231

[16] B. E. Cox, F. K. Loebinger and A. D. Pilkington, JHEP **0710** (2007) 090

[17] J. R. Forshaw, J. F. Gunion, L. Hodgkinson, A. Papaefstathiou and A. D. Pilkington, JHEP **0804** (2008) 090 [arXiv:0712.3510 [hep-ph]].

[18] V. A. Khoze, A. D. Martin and M. G. Ryskin, Eur. Phys. J. C **19** (2001) 477 [Erratum-ibid. C **20** (2001) 599] [arXiv:hep-ph/0011393].

[19] M. G. Albrow and A. Rostovtsev, arXiv:hep-ph/0009336.

[20] B. E. Cox *et al.*, Eur. Phys. J. C **45** (2006) 401 [arXiv:hep-ph/0505240].

[21] V. A. Khoze, M. G. Ryskin and W. J. Stirling, Eur. Phys. J. C **48** (2006) 477 [arXiv:hep-ph/0607134].

[22] T. Aaltonen *et al.* [CDF Run II Collaboration], arXiv:0712.0604 [hep-ex].

[23] T. Aaltonen *et al.* [CDF Collaboration], Phys. Rev. Lett. **99** (2007) 242002

[24] J. M. Butterworth, A. R. Davison, M. Rubin and G. P. Salam, Phys. Rev. Lett. **100**, 242001 (2008) [arXiv:0802.2470 [hep-ph]].

[25] M. Albrow *et al.* [CMS and TOTEM Collaborations], CERN-LHCC-2006-039.

[26] V. A. Khoze, A. D. Martin and M. G. Ryskin, Eur. Phys. J. C **34** (2004) 327

[27] A. G. Shuvaev, V. A. Khoze, A. D. Martin and M. G. Ryskin, arXiv:0806.1447 [hep-ph].

[28] A. Brandt, V. Juranek, A. Pal and M. Tasevsky, Atlas note in preparation.

[29] J. R. Ellis, J. F. Gunion, H. E. Haber, L. Roszkowski and F. Zwirner, Phys. Rev. D **39** (1989) 844.

[30] R. Dermisek, J.F. Gunion. Phys. Rev. Lett. **95** (2005) 041801.

[31] V. A. Khoze, A. D. Martin and M. G. Ryskin, arXiv:0802.0177 [hep-ph].

[32] G. Brown, V. Chavda, A. D. Pilkington and U. Yang, Atlas note in preparation.

[33] A. Brandt *et al.* [UA8 Collaboration], Phys. Lett. B **297** (1992) 417.

[34] V. Barone and E. Predazzi, *High-energy particle diffraction*, Springer, 2002.

[35] S. Alekhin *et al.*, "HERA and the LHC - A workshop on the implications of HERA for LHC physics: Proceedings Part B", arXiv:hep-ph/0601013.

[36] M. Arneodo and M. Diehl, *"Diffraction for non-believers"*, hep-ph/0511047 (2005).
V. A. Khoze, A. D. Martin and M. G. Ryskin,

[37] A. Abulencia *et al.* [CDF Collaboration], Phys. Rev. Lett. **98** (2007) 112001.

[38] V. A. Khoze, A. D. Martin, R. Orava and M. G. Ryskin, Eur. Phys. J. C **19** (2001) 313

[39] J. Favereau de Jeneret, V. Lemaître, Y. Liu, S. Ovyn, T. Pierzchala, K. Piotrzkowski, X. Rouby, N. Schul, and M. Vander Donckt, Eur. Phys. J. C, to be submitted.

[40] K. Piotrzkowski, Phys. Rev. **D63** (2001) 071502.

[41] J. de Favereau, X. Rouby and K. Piotrzkowski, JINST **2**, P09005 (2007) [arXiv:0707.1198 [physics.acc-ph]].

[42] M. Boonekamp, C. Royon, J. Cammin and R. B. Peschanski, Phys. Lett. B **654** (2007) 104 [arXiv:0709.2742 [hep-ph]].

[43] G. Abbiendi *et al.* [OPAL Collaboration], Phys. Rev. D **70** (2004) 032005

[44] N. Schul and K. Piotrzkowski, arXiv:0806.1097 [hep-ph].

[45] J. Ohnemus, T.F. Walsh and P.M. Zerwas, Phys. Lett. B328 (1994) 369-373.

[46] G. Bhattacharya *et al.*, Phys. Rev. D 53, (1996) 2371

[47] M. Drees *et al.*, Phys. Rev. D 50, (1994) 2335

[48] K. Piotrzkowski, hep-ph/9310223

[49] J. Abdallah *et al.* [DELPHI Collaboration], Eur. Phys. J. C31 (2004) 421

[50] G. Abbiendi *et al.* [OPAL Collaboration], Eur. Phys. J. C32 (2004) 453

[51] M. Battaglia *et al.*, Eur. Phys. J. C**33**, (2004) 273.

[52] P.J. Bussey and W. Plano, FPTrack, in preparation.

[53] J. Monk and A. Pilkington, Comput. Phys. Commun. **175** (2006) 232.

[54] See for example: ZEUS and H1 collaborations, AIP Conf. Proc.826:194-199,2006

[55] "LHC Design Report Vol. 1", CERN-2004-003, CERN, Geneva, Switzerland (2004).

[56] A. Aktas *et al.* [H1 Collaboration], Eur. Phys. J. C **51** (2007) 549 [arXiv:hep-ex/0703022].

[57] M. Slater *et al.*, "Cavity BPM tests for the ILC energy spectrometer", SLAC-PUB-13031.

[58] S. Walston *et al.*,

[59] http://meas-spec.com/myMeas/MEAS_download/ApplicationNotes/Position/SchaevitzCernWP_0507.pdf

[60] M. M. Islam, proceedings of the "11th International Conference on Elastic and Diffractive Scattering (Blois Workshop)", 2005

[61] A. Donnachie and P. V. Landshoff, Phys. Lett. B **387** (1996) 637 [arXiv:hep-ph/9607377].

[62] ATLAS Coll., CERN/LHCC/2008-004

[63] T. Columbet, "Cryogenics preliminary calculation for the FP420 cryostat",
https://edms.cern.ch/document/827775.

[64] S. Pattalwar *et al.* "A New Connection Cryostat to insert FP420 Proton Tagging Detectors in the LHC Ring", Proceeds APAC (2007) 103.

[65] R. Folch, "FP420 Cryostat Modules Workpackage",
https://edms.cern.ch/document/823322.

[66] K.Piotrzkowski, U. Schneekloth, Proc. of the ZEUS Collaboration Meeting, March 1994, DESY, Hamburg.

[67] ZEUS Collaboration, S.Chekanov et al., Eur. Phys. J. **C26** (2003) 389.
ZEUS Collaboration, S.Chekanov et al., Eur. Phys. J. **C11** (1999) 35.
H1 Collaboration, A.Aktas et al., Phys. Lett. **B638** (206) 422.

[68] A. Guerrero *et al.*,"CERN front-end software architecture for accelerator controls," (ICALEPCS 2003), Korea, Oct 2003. in Gyeongju 2003, Accelerator and large experimental physics control systems, p. 342.

[69] C. Da Via, J.Hasi, C. Kenney, A. Kok, and S.Parker 3D Silicon detectors. Status an applications. Nuclear Instruments and Methods A Vol 549, pp122-125 Sept. 2005.

[70] V. Berardi *et al.* [TOTEM Collaboration], TOTEM TDR, CERN-LHC-2004-002, Jan 2004.

[71] C. Da Via *et al.*, to be submitted to IEEE Trans. Nucl. Sci.

[72] S.I. Parker and C. J. Kenney, IEEE Trans. Nucl. Sci., **48** (2001) 1629.

[73] C. Da Via *et al.*, to be submitted to IEEE Trans. Nucl. Sci.; and C. Da Via *et al.* presented at the 6th International Symposium on the Development and Application of Semiconductor Tracking Detectors, Carmel (USA), Sept. 11-15 2006.

[74] C.DaVia, S.Parker, G.Darbo, ATL-P-MN-0022,
https://edms.cern.ch/document/828969/1

[75] M. Gilchriese et al., Development of a large area integrated silicon tracking elements for the LHC luminosity upgrade. Proceedings of the 6th Hiroshima Symposium on the development and applications of semiconductor detectors, Nuclear Instruments and Methods A Vol 579, pp801-805 Sept. 2007.

[76] P. Aspell, VFAT2 chip. A front-end system-on-chip providing fast trigger information, digitized strorage and formatting for the charge sensitive readout of multi-channel silicon and gas particle detectors. Prague2007, Electronics for Particle Physics.

[77] E Noschis, PhD Dissertation.

[78] E Noschis et al., Final size Planar Edgeless Silicon Detectors for the TOTEM experiment. NIM A, Vol 563, n1, July 2006 pp 41-44

[79] W. Snoeys, TOTEM project document. Electronics Specification 1/2006.

[80] C. Da Via, Atlas FP 3D silicon detectors, Slides from the Saclay AFP meeting, 19-20 May 2008

[81] C. Da Via et al., 6th International Symposium on the Development and Applications of Semiconductor Tracking Detectors, Sept 11-15 2006, Carmel CA, USA

[82] C. Royon, Internal Note, 7/06, Saclay

[83] K. Gill et al. Radiation hardness qualification of InGaAsP/InP 1310 nm lasers for the CMS experiment. TNS 2002, Vol 49 Issue 6 n1, pp 2923-2929

[84] I. Peric et al., The FEI-3 Readout Chip for the ATLAS pixel detector. Nuclear Instruments and Methods A565 ppp642-671, 2006

[85] ATLAS: Detector and physics performance technical design report. Vol. 1 and 2, CERN-LHCC-99-14/15, ATLAS-TDR-14/15, 1999.

[86] Picosecond Timing Workshop, University of Chicago, March 2008, http://www.hep.anl.gov/ertley/tof/.

[87] M. Akatsu *et al.*, Nucl. Inst. Meth. **A 528** (2004) 763; K. Inami *et al.*, Nucl. Inst. Meth. **A 560** (2006) 303.

[88] Burle http://www.burle.com and Photonis http://www.photonis.com merged in 2005.

[89] J. Milnes, J. Howorth, Proc. SPIE Vol **5580** (2005) 730.

[90] http://www.hamamatsu.com

[91] M.Artuso *et al.*, SUHEP-10-2005, arXiv:physics/0505110.

[92] N. Kishimoto *et al.*, Nucl. Inst. Meth. **A 564** (2006) 204.

[93] S.N. White, arXiv:0707.1500 (hep-ph).

[94] W.E. Cleland and E.G. Stern Signal Processing Considerations for Liquid Ionization Calorimeters in a High Rate Environment, Nuclear Instruments and Methods, Vol. 338 pp 467 1994.

[95] E. Delagnes, Y. Degerli, P. Goret, P. Nayman, F. Toussenel, and P. Vincent. SAM : A new GHz sampling ASIC for the HESS-II Front-End. Cerenkov 2005

[96] Design and Performance of the 5GHz Waveform Digitizer Chip DRS3, Submitted to Nuclear Instruments and Methods, Nov. 2007.

[97] Gary Varner, L.L. Rudman, J.W. Nam, R.J. Nichol, J. Cao, P.W. Gorham, and M. Wilcox. The Large Analog Bandwidth Recorder And Digitizer with Ordered Readout (LABRADOR) ASIC, submitted to Elsevier Science, Feb 2008.